

Targeting G-quadruplexes in the rhinovirus genome by Pyridostatin inhibits uncoating and highlights a critical role for sodium ions.

Antonio Real-Hohn (✉ antonio.hohn@meduniwien.ac.at)

Vienna Biocenter, Max Perutz Laboratories, Medical University of Vienna <https://orcid.org/0000-0003-0334-2877>

Martin Groznica

Vienna Biocenter, Max Perutz Laboratories, Medical University of Vienna

Georg Kontaxis

Vienna Biocenter, Max Perutz Laboratories, University of Vienna

Rong Zhu

Johannes Kepler University Linz

Otávio Chaves

Immunopharmacology Laboratory, Oswaldo Cruz Institute (IOC/Fiocruz)

Leonardo Vazquez

Immunopharmacology Laboratory, Oswaldo Cruz Institute (IOC/Fiocruz)

Peter Hinterdorfer

Johannes Kepler University of Linz <https://orcid.org/0000-0003-2583-1305>

Dieter Blaas

Medical University of Vienna <https://orcid.org/0000-0002-9612-3376>

Heinrich Kowalski

Vienna Biocenter, Max Perutz Laboratories, Medical University of Vienna

Article

Keywords: rhinovirus genome, G-quadruplexes, sodium ions

Posted Date: July 8th, 2021

DOI: <https://doi.org/10.21203/rs.3.rs-646190/v2>

License:   This work is licensed under a Creative Commons Attribution 4.0 International License.

[Read Full License](#)

1
2 **Targeting G-quadruplexes in the rhinovirus genome by Pyridostatin inhibits uncoating**
3 **and highlights a critical role for sodium ions.**
4

5 Antonio Real-Hohn^{1*}, Martin Groznica¹, Georg Kontaxis², Rong Zhu³, Otávio Augusto
6 Chaves⁴, Leonardo Vazquez⁴, Peter Hinterdorfer³, Dieter Blaas¹, and Heinrich Kowalski^{1*}
7

8 ¹Vienna Biocenter, Max Perutz Laboratories, Medical University of Vienna, Center of Med.
9 Biochemistry, Dr. Bohr Gasse 9/3, A-1030 Vienna, Austria; ²Vienna Biocenter, Max Perutz
10 Laboratories, University of Vienna, Department of Structural and Computational Biology,
11 Campus Vienna BioCenter 5, A-1030 Vienna, Austria; ³Institute of Biophysics, Johannes
12 Kepler University Linz, Gruberstr. 40, A-4020 Linz, Austria; ⁴Immunopharmacology
13 Laboratory, Oswaldo Cruz Institute (IOC/Fiocruz), Av. Brasil 4365, 21040-360 Rio de
14 Janeiro, Brazil.
15

16 * Correspondence: antonio.hohn@meduniwien.ac.at; heinrich.kowalski@meduniwien.ac.at.
17

18 **ABSTRACT**

19 The ~2.4 μm long rhinovirus ss(+)RNA genome consists of roughly 7,200 nucleotides.
20 It is tightly folded to fit into the ~22 nm diameter void in the protein capsid. In addition to
21 previously predicted secondary structural elements in the RNA, using the QGRS mapper, we
22 revealed the presence of multiple quadruplex forming G-rich sequences (QGRS) in the RV-
23 A, B, and C clades, with four of them being exquisitely conserved. The biophysical analyses
24 of ribooligonucleotides corresponding to selected QGRS demonstrate G-quadruplex (GQ)
25 formation in each instance and resulted in discovering another example of an
26 unconventional, two-layer zero-nucleotide loop RNA GQ stable at physiological conditions.
27 By exploiting the temperature-dependent viral breathing to allow diffusion of small
28 compounds into the virion, we demonstrate that the GQ-binding compounds PhenDC3 and
29 pyridostatin (PDS) uniquely interfere with viral uncoating. Remarkably, this inhibition was
30 entirely prevented in the presence of K⁺ but not Na⁺, despite the higher GQ stabilising effect
31 of K⁺. Based on virus thermostability studies combined with ultrastructural imaging of isolated
32 viral RNA, we propose a mechanism where Na⁺ keeps the encapsidated genome loose,
33 allowing its penetration by PDS to promote the transition of QGRS sequestered in alternative
34 metastable structures into GQs. The resulting conformational change then materialises in a
35 severely compromised RNA release from the proteinaceous shell. Targeting extracellularly

36 circulating RVs with GQ-stabilisers might thus become a novel way of combating the
37 common cold.

38 INTRODUCTION

39 Rhinoviruses (RVs) are the etiologic agents of the common cold, a usually mild upper
40 respiratory illness. Nevertheless, RVs are increasingly found also to cause severe lower
41 respiratory tract diseases ^{1, 2}. Due to the lack of vaccines and effective treatment options,
42 their socio-economic impact through lost working days and cost of symptom-alleviating
43 medication is in the order of billions per year in the USA alone ^{3, 4}. Belonging to the family
44 *picornaviridae*, RVs are built from 60 copies of each four capsid proteins (VP1 through VP4)
45 that enclose a single-stranded ~7.2 kb long (+) RNA genome. VPg, a 21 amino acid long
46 peptide, is covalently linked to its 5'-end via a tyrosine phosphodiester bond, and a genome-
47 encoded poly-(A) tail extends its 3'-end. Infection initiates upon recognition of cell-surface
48 receptors. These include the low-density-lipoprotein receptor (LDLR) and related proteins,
49 intercellular adhesion molecule 1 (ICAM-1), and cadherin-related family member 3 (CDHR3),
50 depending on the RV-receptor group (minor or major) and the RV species (A, B, or C).
51 Currently, more than 170 RV types are known [[https://talk.ictvonline.org/ictv-
52 reports/ictv_online_report/positive-sense-rna-
53 viruses/picornavirales/w/picornaviridae/681/genus-enterovirus](https://talk.ictvonline.org/ictv-reports/ictv_online_report/positive-sense-rna-viruses/picornavirales/w/picornaviridae/681/genus-enterovirus)].

54 Upon uptake into the host cell by receptor-mediated endocytosis, the native RV
55 particle (~30 nm diameter) converts into the expanded (i.e. altered) A-particle (~31.2 nm
56 diameter) with holes at the 2- and 3-fold axes of icosahedral symmetry. This conformational
57 change is triggered by the endosomal acidic pH and/or the viral receptor. Concomitant with
58 expansion, VP4 is lost, N-terminal amphipathic sequences of VP1 are externalised, and
59 contacts between the RNA and the inner wall of the capsid become modified ^{5, 6}. Data on the
60 closely related poliovirus and enterovirus 71 ^{7, 8} suggest that the viral genome, in the form of
61 a single strand, exits through a hole in the capsid, which is tightly connected to a pore in the
62 endosomal membrane, thereby forming an RNase-inaccessible channel ^{9, 10}. On the other
63 hand, *in vitro* studies with acidified echovirus 18, another member of the *Enterovirus* genus,
64 have shown that entire pentamers of coat protein detach from the capsid, giving rise to large
65 holes allowing for the exit of incompletely unfolded RNA ¹¹. The same group also observed
66 about 7 % of such open particles in a very recent cryo-EM analysis of ICAM-1 triggered
67 uncoating of RV-B14 in combination with a low pH ¹².

68 On arrival of the RV genome in the cytosol, the VPg is removed by a cellular
69 unlinkase activity, and the RNA used as a template for an internal ribosomal entry site (IRES)
70 directed translation by host cell ribosomes. The resulting polyprotein is co-translationally and
71 autocatalytically processed by the viral proteinases 2A^{pro} and 3C(D)^{pro} into structural and

72 non-structural proteins¹³. Viral proteins such as 2C and 3A together with recruited host cell
73 proteins including lipid kinases build the replication complex (RC), which is intimately
74 associated with the outer surface of virus-induced single and double-membrane vesicles.
75 These are the sites for the production of (–) ssRNA, in turn serving as a template for the
76 production of multiple copies of (+) ssRNA in separate RCs, both mediated by the viral RNA-
77 dependent RNA polymerase 3D^{pol}. The newly produced (+) ssRNAs are used for further
78 translation, the synthesis of additional (–) ss RNAs, or for packaging into provirions, followed
79 by a rapid maturation cleavage of their immature capsid protein VP0 into VP2 and VP4. The
80 resulting progeny virions are then released by lytic and non-lytic mechanism from the
81 infected host cell (reviewed in^{14, 15}).

82 Up to date, no vaccines are available against RVs and in the absence of approved
83 antiviral drugs the therapeutic treatment is centred on the relief of the common cold
84 symptoms. One prominent route in developing new antiviral drugs is targeting viral proteins
85 or host factors vital for the virus replication (e.g. Baggen, Thibaut¹⁶). However, targeting viral
86 polypeptides often results in the rapid emergence of drug-resistant mutants, while
87 compounds acting against host factors may give rise to substantial cellular toxicity. An
88 alternative approach targets essential domains in the highly structured genomes of RNA
89 viruses, limiting the development of resistance¹⁷. In that context, G-quadruplexes (GQs)
90 have recently emerged as promising antiviral drug targets¹⁸.

91 GQs are 4-stranded higher-order nucleic acid structures formed intra- or
92 intermolecularly by guanine (G) rich stretches of DNA or RNA. The basic unit consists of a
93 square, co-planar arrangement of four guanines (a tetrad or G-quartet) connected via
94 Hoogsteen hydrogen bonding. Their self-stacking via π - π interactions results in a GQ with
95 minimally two layers. A cation inserted between or in the centre of the tetrads, dependent on
96 its ionic radius, further stabilises the structure. The core guanines are linked by three nucleic
97 acid sequences (loops) of varying composition, topology, and size. The overall stability of
98 individual GQs is governed by the number of layers, length and identity of the loops, the
99 flanking nucleotides and the concentration and type of bound cation. In contrast to DNA
100 GQs, RNA GQs are practically monomorphic, displaying (with a few exceptions^{19, 20}) all
101 strands oriented in parallel, and are preferentially stabilised by potassium ions (K⁺) binding
102 between adjacent tetrads²¹. Higher-order structures may further result from 5'–5' or 3'–3'
103 stacking of the terminal quartets of individual GQs.

104 GQs have been identified in all domains of life and have been implicated in a large
105 number of critical biological processes, including transcription, translation, epigenetic
106 regulation, DNA recombination, splicing, and mRNA transport^{22, 23}. These unconventional
107 secondary structures are also found in the genome of DNA and RNA viruses such as Ebola
108 virus, herpes simplex virus, human papillomavirus, human immunodeficiency virus, Zika

109 virus, Influenza virus, human coronaviruses, and hepatitis C virus^{24, 25, 26, 27, 28, 29, 30, 31}, where
110 they control various steps in the virus life cycle, ranging from the expression and replication
111 of their genetic material to the assembly into protective nucleocapsids¹⁸. In an increasing
112 number of examples, it was found that GQ-stabilising compounds such as pyridostatin
113 (PDS), PhenDC3, Braco19 and others inhibited viral replication at the level of transcription,
114 translation, and/or genome replication. This has been related to a stabilisation of certain GQs
115 in the genome or transcripts of these pathogens acting e.g., as physical road blocks for virus-
116 and/or host cell-encoded enzymes such as DNA and RNA polymerases or the ribosomes.
117 Alternatively, these compounds were also found to compete with the host cell or viral
118 proteins for binding to these structures with frequently inhibitory but occasionally also
119 stimulatory effects on their reproduction^{32, 33}.

120 Up to date, nothing is known about a possible role of these unconventional secondary
121 structures in picornaviruses. We have therefore initiated such study with RV-A2 as a model.
122 In infectivity studies, we find that the GQ ligands PDS and PhenDC3 specifically inhibit the
123 uncoating of the viral RNA, which has not yet been described for any virus. Using a broad
124 combination of biophysical and ultrastructural analysis, we demonstrate the conversion of
125 metastable alternative structures retained in the viral RNA into GQ promoted by PDS. This,
126 in turn, results in a conformational change most likely underlying the defective RNA release
127 from the capsid. Strikingly, the process is critically governed at the level of the genomic RNA
128 compaction by the prevalent alkaline cation (K^+ , Na^+) present in the capsid, with K^+ drastically
129 limiting PDS access. These results show that targeting of GQs might open up an entirely new
130 avenue for combating the common cold viruses during their dissemination in the sodium-rich
131 extracellular fluids.

132

133 RESULTS

134 QGRS-mapper identifies potential GQ-forming sequences in all RV genomes.

135 Employing extensive bioinformatics analysis, Lavezzo and colleagues recently
136 predicted GQs in viral genomes of human virus species, including RVs³⁴. We independently
137 confirmed and extended their findings for all RV genome sequences available in Genbank
138 by using a local copy of the same program that runs on the quadruplex-forming G-rich
139 sequence (QGRS) mapper web-based server³⁵. This software has been originally developed
140 to identify putative QGRS in DNA, where the G-score reflects the stability of a predicted GQ,
141 which usually increases with the number of G-tetrad and decreases with the loop size. The
142 respective search motif $G_{\geq 3}L_{1-7}G_{\geq 3}L_{1-7}G_{\geq 3}L_{1-7}G_{\geq 3}$ takes into account that most experimentally
143 identified DNA GQs conformed to short-looped (1 to 7 nucleotides) structures with three and
144 occasionally more G-tetrad. However, RNA GQs are generally more stable than the

145 corresponding DNA GQs ³⁶; two-layer RNA GQs are therefore not uncommon ³⁷, and the
146 overall higher stability of RNA GQs allows the insertion of larger loops compared to DNA
147 GQs ^{38, 39}. Recently, an atypical RNA GQ with no first loop has been described ³⁷. Therefore,
148 we adjusted the search parameters of the QGRS mapper to allow the identification of
149 putative unconventional long-loop and zero-nucleotide loop G-quartets, including those
150 featuring only two layers. We then plotted the respective QGRS prediction G-scores ≥ 10
151 against their positions in the genomic RNA sequences (Fig. 1a). Strikingly, the vast majority
152 of rhinoviral genomes feature only QGRS predicted to form just two-layered GQs. RV-A41
153 and RV-B4 are singled out by the additional presence of one and two three-layer GQs,
154 respectively.

155 Furthermore, most RV-ABC genomes feature at least one and up to seven putative
156 zero-nucleotide loop GQs without marked conservation. The number of potential QGRS
157 varies from 6 to 19 (mean 12) for the RV-As, from 9 to 19 (mean 13) for the RV-Bs, and from
158 10 to 23 (mean 15) for the RV-Cs. The augmented prevalence of QGRS for the RV-C
159 species is likely attributable to their genomes' distinctly higher GC content (43 % for RV-C,
160 38 % for RV-A, and 38 % for RV-B ⁴⁰). The analysis further revealed four highly conserved
161 QGRS (Fig. 1a - asterisk), all located in the open reading frame. The slight differences in
162 their position between the genera (RV-A, RV-B, and RV-C) result from clade-specific
163 insertions and deletions. An additional conserved QGRS is uniquely present in the RV-Bs,
164 upstream and close to the second highly conserved QGRS motif. By contrast, only
165 moderately conserved QGRS were predicted in the 5' untranslated region (UTR), which
166 comprises essential regulatory elements such as the 5' cloverleaf structure and the IRES,
167 required for replication and cap-independent translation ⁴¹. No single QGRS was predicted
168 within the short 3' UTR, featuring a highly conserved hairpin involved in virus replication ⁴².

169

170 **NMR analysis demonstrates the folding of synthetic ribooligonucleotides representing** 171 **selected QGRS of RV-A2 RNA into GQs, which is differentially affected by PDS.**

172 For RV-A2, QGRS-mapper predicted 11 QGRS with G-score ≥ 10 (Supplementary
173 Fig. S1). We chose to study the candidates with the lowest and highest G-scores, G11 and
174 G20, the latter also representing one of the four highly conserved GQs (see above).
175 Assuming the almost invariable adoption of parallel GQs by RNA, G11 would give rise to an
176 unusual monomeric two-layer GQ bearing a zero-nucleotide loop 3 in combination with a
177 long loop 1 (Table 1; a schematic illustration of the likely G11 and G20 RNA GQ structure is
178 displayed in Supplementary Fig. S1). To confirm their GQ-forming propensity, we collected
179 ¹H NMR spectra using 250 μ M of the derived synthetic ribooligonucleotides in 10 mM sodium
180 phosphate (pH 7.4), 100 mM KCl, similarly as described elsewhere ⁴³. Each ribonucleotide
181 was denatured at 95 °C for 10 min, followed by cooling to 4 °C for 10 min to favour

182 intramolecular annealing into GQ and possibly other secondary structure(s) in the presence
183 of monovalent cations. A high concentration of K^+ usually stabilises GQs, as shown in other
184 instances³⁶. G11 and G20 displayed 1H signals of the bulk of the imino proton in the region
185 between 10.4 – 12.4 ppm, which is the typical NMR signature of GQs (Fig. 1b – salmon-
186 coloured area). The lack of sharp signals can be explained by G-register exchange dynamics
187⁴⁴ since certain G runs have more than two Gs, indicating the possible presence of
188 alternative conformations.

189 Peaks in the canonical Watson-Crick base pair region at 1H NMR shifts larger ~12.4
190 ppm (olive-coloured area) are observable at low (4 °C) but not at high temperatures (34 °C,
191 the optimal temperature for RV-A2 replication), indicating that these secondary structure
192 elements (presumably hairpin(s)) are less stable than the GQs. Within the range assigned to
193 GQs, the second peak (11.9 – 12.4 ppm) observed only for G11 (Fig. 1b) exhibited unaltered
194 intensity in an HDX experiment performed for 7 h at 37 °C. The solvent inaccessibility of
195 these imino protons indicated that they were most likely also part of the GQ core
196 (Supplementary Fig. S2a). In the G20 spectrum, three distinct peaks (one within and two
197 next to the upfield broader of the GQ region) completely disappeared with increasing
198 temperature, indicating that the corresponding imino protons are conceivably not
199 involved in the G-tetrad core formation. The addition of 500 μM pyridostatin (PDS), which
200 specifically binds with high affinity to DNA and RNA GQs but not to other nucleic acid
201 secondary structures except i-motif forming DNA⁴⁵, resulted in substantial changes of the
202 imino 1H peaks for both synthetic RNAs (Fig. 1b and Supplementary Fig. S2b), indicative of a
203 specific interaction.

204 The only other 1H -NMR study we are aware of using PDS and a GQ was performed
205 with a three-layer DNA GQ derived from the src kinase gene (SRC). This showed an upfield-
206 shifting of GQ imino proton signals stemming from PDS binding to the top G-quartet in a
207 stacking mode⁴⁶. However, the differential effect observed by us suggested that the binding
208 mode of PDS may vary for G11 vs G20. We hence used molecular docking to assess this
209 possibility further. For lack of detailed structural information about the G11/G20 system, we
210 instead *in silico* evaluated the interaction of a crystallographic model of a pseudorabies virus
211 RNA GQ molecule composed of two G-quartets (PQS18-1, GGCUCGGCGGCGGA) (PDB
212 6JJH⁴⁷) and PDS. Using increasing concentrations of PDS in this *in silico* analysis, we
213 unexpectedly discovered that it could form defined dimers mostly stabilised by π - π
214 interactions. This was then experimentally substantiated by UV-absorption spectroscopy,
215 which clearly demonstrated a concentration-dependent self-association of PDS (K_a ~42 μM)
216 in the buffer chosen for NMR spectroscopy (Supplementary Fig. S3).

217 The analysis of the best docking poses for the monomeric and dimeric PDS and
218 PQS18-1 revealed two distinct classes of binding modes (Supplementary Fig. S4): i) end-

219 stack (a and c), and ii) groove/loop-binding (b and d). In both instances, the 2-(quinolin-4-
 220 oxy)ethanamine moiety of PDS interacts with the nucleobases via Van der Waals forces and
 221 an additional contribution of electrostatic interactions between the charged amino groups of
 222 PDS structure and the phosphate groups of the GQs. These binding modes may be variably
 223 exploited for the interaction with G11 and G20, presumably resulting in the idiosyncratic
 224 PDS-induced peak shifts.

225 Altogether, these results provided the initial bioinformatics analysis demonstrating the
 226 likely formation of two-layered GQs by both ribooligonucleotides under favourable conditions
 227 for the folding of such structures.

228

Ribooligonucleotides	Sequence
Negative Control	5'- UUA CCC UUA CCC UUA CCC UUA CCC UUA -3'
miniTERRA (G-score = 42)	5'- UUA G GG UUA G GG UUA G GG UUA G GG UUA -3'
G11 (position 2048 – 2074)	5'- G GC ACU CAU GUU AUA UGG GAU GUG G GG -3'
G20 (position 1038 – 1064)	5'- CCU CAA A GG GUU G GU G GU G GA AAC UAC -3'

229

230 Table 1 – Sequences of the synthetic ribooligonucleotides used in this study. Note that in the
 231 negative control, all Gs of miniTERRA were replaced by Cs.

232

233 **Circular dichroism spectroscopy of the synthetic ribooligonucleotides G11 and G20** 234 **reveals a parallel GQ folding topology.**

235 We next verified the tentatively assigned folding topology of G11 and G20 by circular
 236 dichroism (CD) spectroscopy. CD is a gold standard to determine the strand orientations of
 237 GQs. These might be parallel, as commonly adopted by RNA and DNA, or anti-parallel and
 238 hybrid, which, with a few exceptions⁴⁸, are observed only for DNA. Telomeric-repeat-
 239 containing RNA (miniTERRA; Table 1), which adopts a three-layer parallel conformation⁴⁹,
 240 served as a positive control.

241 The CD profiles of miniTERRA, G11, and G20 taken at 25 °C in either 100 mM
 242 sodium or 100 mM potassium phosphate buffer (pH 7.4) in each instance displayed the
 243 signature of an all-parallel topology (ellipticity shows a negative band at 240 nm and a
 244 positive band at 265 nm). The monovalent Na⁺ and K⁺ cations differentially stabilise GQs
 245 owing to their different ionic radius and hydration free energies⁵⁰. Generally, potassium
 246 promotes folding and stabilises (ribo)oligonucleotide GQs to a larger extent than sodium^{36, 51},
 247 though some exceptions have been reported⁵². In accordance with the latter, the degree of
 248 GQ formation of G20 was noticeably the same irrespective of the presence of Na⁺ or K⁺ as
 249 indicated by the practically unchanged CD spectrum (Fig. 1c). By contrast, as found for the
 250 vast majority of GQ forming RNAs, the miniTERRA control and the G11 ribooligonucleotide

251 showed a higher proportion of GQ structure in K^+ compared to Na^+ . The trough at 210 nm
252 only evident for G11 and G20 is likely attributable to the additional presence of structural
253 elements comprising A-type duplex RNA regions as also revealed in the above NMR
254 analysis at low temperature.

255 **Na^+ and K^+ differently impact the physicochemical parameters of G11, G20, and**
256 **miniTERRA ribooligonucleotides.**

257 As seen in Figure 2a, the CD melting and annealing spectra are almost
258 superimposable for the G11 and G20 ribooligonucleotides and the miniTERRA control when
259 dissolved in a sodium-containing buffer. The lack of a marked hysteresis indicates
260 thermodynamic equilibrium between denaturation and refolding in the examined temperature
261 range and the used ramp rate and is typical for intramolecular GQs⁵³. The situation for
262 miniTERRA was strikingly different in the potassium buffer, where the unfolding/annealing
263 profiles exhibited a marked hysteresis (Fig. 2a); this is typically observed for intermolecular
264 GQ formation, where the shape of the melting and refolding curves depends on the speed of
265 temperature ramping⁵³. Another possibility is a slow conformational change of an
266 intramolecular GQ from one topology to another⁵⁴. However, according to CD spectroscopy,
267 miniTERRA in the presence of either cation (Na^+ , K^+) formed a parallel GQ (Fig 1c)
268 exclusively. Since the multimerisation of miniTERRA could be ruled out by a subsequent
269 electrophoretic analysis (see below), the relatively slow ramp rate of 1 °C/min apparently still
270 did not allow the reversible refolding of this three-layer intramolecular GQ. This is in line with
271 findings by others that multiple layers of tetrads are particularly prone to hysteresis⁵⁵. By
272 contrast, in the presence of K^+ , the CD melting/cooling profiles of both two-layered GQs
273 exhibited just a rather subtle (G11) to negligible hysteresis (G20). The latter's overlapping
274 heating and cooling curves, as also seen with Na^+ buffer, reinforces the notion that G20
275 forms a monomeric (see below) intramolecular GQ in presence of each of these cations.

276 Others have shown that K^+ -containing solutions stabilise the parallel topologies of
277 two- and three-quartet RNA GQ much more than Na^+ -containing solutions, with the
278 difference in the melting temperatures ΔT_m ranging from 15 to more than 30 °C^{36, 51}. Such
279 drastic change in T_m (determined at the intersection of the second derivative with the x-axis
280 in Fig 2a) was also evident for the three-layer miniTERRA GQ in K^+ compared to Na^+ . By
281 contrast, the melting temperatures of G11 and G20 in the K^+ containing buffer were just ~ 4
282 °C higher than those determined in Na^+ buffer.

283 The limited hysteresis of G11 melting/cooling might indicate the formation of a dimeric
284 GQ resulting from end-to-end stacking of two intramolecular GQs. This gains additional solid
285 support from native gel electrophoresis, which clearly shows the occurrence of dimers in the
286 presence of potassium ions for G11. Under these conditions, G20 and the miniTERRA
287 control gave rise to just a single band, indicating that they existed primarily as monomers

288 (Supplementary Fig. S5). Based on these results, the slight hysteresis of the G11 melting
289 can be best interpreted by assuming a fast monomer refolding, followed by slower
290 oligomerisation.

291 The adoption of a GQ conformation by the two RV-A2 derived RNA sequences (G11
292 and G20) and the positive control (miniTERRA) was then confirmed with a Thioflavin T (ThT)
293 light-up assay with all measurements done at room temperature. ThT end-stacks to RNA
294 GQs, which strongly increases its fluorescence⁵⁶. As seen in Fig. 2b and 2c, no significant
295 fluorescence was detected upon incubation with the negative control (C for G substituted
296 miniTERRA) ribooligonucleotide (see Table 1). In contrast, a clear signal was obtained for all
297 three tested GQs, whose magnitude was quite comparable for G11 in Na⁺ (left panel of Fig.
298 2b) and K⁺ buffer and about 1.5 and 2-fold higher in the presence of K⁺ for miniTERRA and
299 G20, respectively (left panel of Fig. 2c). The ThT fluorescence intensity was strongest for
300 miniTERRA and approximately 3 to 4-fold lower for G11 and G20 (but still 30 to 40 times
301 higher than for the negative control), roughly correlating with their respective G-scores. Since
302 the same amounts of oligonucleotides were employed, this indicated that a fraction of G11
303 and G20 adopted a non-GQ conformation as already observed in the ¹H-NMR analysis. The
304 coexistence of A-type RNA (hairpin) structure and a two-layer GQ structure has been
305 recently described by Lightfoot and others³⁷. Based on the ThT light-up probe, G11, but not
306 G20 would be almost indifferent to the choice of the two cations, which is opposite to the
307 results of the label-free CD analysis. Most likely, the conformation of the respective GQs
308 subtly differs when bound to Na⁺ (which coordinates with the Gs in the middle of a tetrad) or
309 K⁺ (residing between G-tetrads), which may variably affect the binding affinity for ThT giving
310 e.g. the impression of an apparent higher stability of G20 in K⁺ buffer. However, this does not
311 change our overall conclusion that GQ structures are formed with both cations in this assay.

312 We then examined whether the tetrad-associated cation type (K⁺ or Na⁺) impacts the
313 interaction of the respective GQs with PDS by conducting a fluorescent indicator
314 displacement (FID) assay, similar to the one described in refs.^{57, 58}. FID allows evaluating the
315 relative affinity and selectivity of compounds binding to a GQ⁵⁹. Expectedly, ThT was
316 displaced by PDS in each instance (right panels in Fig. 2b/c). However, while the dose-
317 response curve for miniTERRA was comparable in Na⁺ and K⁺ containing buffers, the
318 reduction in fluorescence determined for G11 and G20 was about 2-fold more efficient in the
319 presence of Na⁺ as indicated by the respective IC₅₀ values (Table 2). Notably, with the lower
320 G-scoring G11, a sharp decrease of the ThT fluorescent signal was already evident at low
321 PDS concentrations. Since ThT was shown not to markedly alter the stability of GQs⁶⁰, this
322 might indicate a higher affinity of PDS for the noncanonical GQ-forming G11 in comparison
323 to miniTERRA and G20 as reflected by the correspondingly lowest IC₅₀ values (Table 2).

324

325

Ribooligonucleotides	IC ₅₀ (μM)		Significance
	Na ⁺	K ⁺	
mini TERRA	19.3 ± 0.5	17.5 ± 0.7	NS
G11 (position 2048 – 2074)	2.8 ± 1.4	6.1 ± 1.1	p<0.0001
G20 (position 1038 – 1064)	10.5 ± 5.2	20.3 ± 1.0	p<0.001

326

327 Table 2 – IC₅₀ values for the displacement of ThT by PDS. Significance determined by using
328 ANOVA with Tukey's multiple comparison test.

329

330 **Pyridostatin (PDS) and PhenDC3 reduce RV-A2 infectivity.**

331 Taken together, employing several orthogonal assays, we could demonstrate the
332 intrinsic ability of two selected RV-A2-derived QGRS to form RNA GQs. However, within the
333 context of the viral RNA, these and the other predicted candidate sequences may fail to fold
334 into such scaffolds if embedded into or overlapping with alternative secondary structures of
335 higher stability or more rapid formation (and trapped in a metastable state). Furthermore, the
336 G-quartet fold of some untested putative QGRS may be too unstable at the temperature of
337 virus propagation. PDS and other so-called GQ-stabilising compounds can selectively
338 enhance the mechanical and thermal stability of DNA and RNA GQs over the level achieved
339 by K⁺ alone^{61, 62}. Thereby, they can also force alternative secondary structures to transform
340 into the compound-stabilised quadruplex conformation⁶³. The latter was evident for G20 and,
341 less pronounced, for G11 by the loss of Watson-Crick peaks in the ¹H-NMR spectrum on
342 incubation with PDS (Supplementary Fig. S2b).

343 It is presently believed that the uncoating of RV-A2 and several other enteroviruses
344 requires a structural switch of the genomic RNA and the transient unfolding of secondary
345 structures for transit as a single-strand through one of the narrow pores formed in the A-
346 particles^{5, 7, 64, 65, 66}. Therefore, we reasoned that the exposure of the encapsidated viral RNA
347 to PDS by stabilising preexisting GQs and promoting the transition of unstructured and/or
348 alternatively folded QGRS into such unconventional secondary structures might interfere with
349 its *in vitro* and *in vivo* uncoating. RVs, in contrast to other enteroviruses such as poliovirus,
350 are readily permeable for monovalent cations such as Cs⁺ already in the cold and also for
351 small organic compounds such as dansylaziridine and ribogreen when incubated at
352 breathing conditions^{67, 68, 69}. Capsid breathing describes a transitory expansion of the protein
353 shell with temporary exposure of normally internal amino acid sequences through reversibly
354 formed small holes, commencing at room temperature to around physiological temperatures,
355 dependent on the RV serotype⁷⁰. We thus attempted to deliver PDS to the viral RNA
356 genome within the native virion by exploiting this phenomenon. All incubations were done in

357 phosphate-buffered saline (PBS) to prevent PDS aggregation into long fibrils, as we have
358 recently observed for Tris- but not phosphate-based buffers ⁷¹.

359 First, we confirmed the dependence of PDS delivery to the inside of the capsid as a
360 function of temperature. Purified RV-A2 was incubated with PDS under conditions of strongly
361 diminished capsid breathing (at 4 °C) and a capsid breathing-promoting temperature (at 34
362 °C). Unbound PDS was removed, and a **Particle Stability Thermal Release Assay (PaSTRy)**
363 ^{72, 73} was performed to determine a possible impact of PDS on temperature-dependent
364 uncoating, a commonly used model for *in vitro* uncoating of picornaviruses ⁷⁴. Fig. 3a shows
365 the temperatures where the genomic RNA becomes accessible to SYTO 82 as deduced from
366 the temperature vs fluorescent emission curves ⁷³ (Supplementary Fig. S6). Virus pre-
367 incubated with PDS at 34 °C exhibited a striking 4.7 °C earlier onset of genomic RNA
368 accessibility to SYTO 82 compared to the control condition, i.e., incubation with PDS at 4 °C
369 (to prevent diffusion of this compound through the protein shell) (T_{on} of 37.7 °C vs. 42.4 °C).
370 However, the temperatures T_{max} at the peak of the SYTO 82 signal (indicative of the
371 complete conversion of all native virions into permanently porous A-particles) and the peak of
372 the first derivative (at T_{50} , corresponding to 50 % RNA accessibility) ⁷³ remained practically
373 unaltered.

374 We interpret this finding as that PDS, by interacting with (potential) QGRS in the
375 genome of RV-A2, directly or indirectly affected RNA contacts with the capsid, thereby
376 resulting in enhanced mobility of the protein shell of the native virus. This allowed
377 appreciable uptake of the SYTO 82 dye into the viron for binding the viral RNA already at a
378 lower temperature compared to the control. However, the PDS-induced effect did not
379 critically impact the rate of the temperature-dependent conversion of native to A-particle as
380 inferred from the unchanged T_{50} for this sigmoidal conversion ⁷³. The heat-triggered RNA
381 release starting at T_{max} (resulting in the subsequent drop of the SYTO 82 signal) was also not
382 affected. As thermal unzipping of secondary structures is required for the exit of the RNA
383 from the capsid in this *in vitro* uncoating model ⁶⁴, the bound PDS evidently did not increase
384 the melting temperature of the viral GQs above one of the most stable non-GQ secondary
385 structures (presumably mostly hairpin loops ⁷⁵) inside the capsid.

386 We then assessed the effect of PDS on the *in vivo* uncoating of RV. HeLa cells were
387 infected with RV-A2 pre-incubated with PDS and without PDS (control), both at 34 °C for 4 h.
388 This treatment time sufficed for the entry of appreciable amounts of RiboGreen into the
389 capsid of RV-A2 ⁶⁹. Unbound PDS was removed by centrifugation in an Amicon ultrafilter
390 unit, followed by repeated washing with PBS at 25 °C. The viral samples were then
391 transferred to HeLa cells grown in 10 cm diameter dishes and incubated for 30 min to allow
392 for viral uptake and uncoating in the absence of inhibitory compounds ⁶⁵. Supernatant and
393 cells were collected by scraping, and internalised viral material was recovered by five times

394 freezing and thawing. Cell debris was removed, and aliquots of the supernatants were
395 subjected to immunoprecipitation with the subviral (A- and B-particle) specific monoclonal
396 antibody 2G2^{76, 77}. From equal aliquots of the precipitated material, protein and RNA were
397 recovered and quantified in Western blots (Fig. 3b) and by RT-qPCR, respectively (Fig. 3c).
398 Comparing these results, it becomes clear that regardless of whether the pre-incubation was
399 carried out in the presence or absence of PDS, the same amount of viral proteins were
400 detected. This excludes any influence of PDS on cell attachment, e.g. via forming virus-
401 trapping filaments as observed in Tris-based buffers (see above and ref.⁷¹) or on the overall
402 rate of native to subviral (A + B) particle conversion. However, quantification of the viral RNA
403 contained in the 2G2 precipitates showed that the virus incubated in the presence of PDS
404 and recovered from cells 30 min post-infection (pi) in the form of subviral A- and B-particles
405 contained about 70 % more viral RNA than virus pre-incubated without PDS. This can be
406 taken to indicate that significantly less RNA was released from the endocytosed PDS-treated
407 virus during the first 30 min following the challenge of the cells.

408 Thirty min pi aliquots from similarly infected cells (as above) were also analysed by
409 sedimentation through preformed sucrose density gradients. Ultracentrifugation under the
410 specified conditions allows for separating native virus, A-particles, and empty B-particles⁷⁸.
411 The profile in Fig. 3d verifies the presence of mostly B-particles sedimenting at 80S for the
412 virus subject to control conditions (- PDS). In stark contrast, a substantial fraction of the virus
413 treated with PDS shifted towards higher sedimentation rates with a peak in-between 150S
414 (where the native virus sediments) and 80S, corresponding to (viral RNA containing) A-
415 particles (hash). These results again point to a substantial impairment of *in vivo* RNA release
416 by the incorporated PDS.

417 The observed effect of PDS in the PaSTRY assay and on the *in vivo* uncoating of RV-
418 A2 was most likely due to the trapping/stabilisation of GQs located in the encapsidated RNA
419 rather than an unspecific binding to other components of the virion. However, in one report,
420 PDS was found to act as a weak inhibitor of the C5 convertase, a component of the
421 complement system⁷⁹. Therefore, to further furnish our hypothesis, we repeated the *in vivo*
422 analysis at capsid breathing conditions with another frequently used GQ-binding compound,
423 Phen-DC3⁸⁰. RV-A2 was incubated as described above with PDS at 20 μ M and 200 μ M and
424 in parallel with PhenDC3 at 1 μ M and 5 μ M, respectively. A mock-treated virus was used as
425 a control. All samples were subjected to repeated centrifugal ultrafiltration to remove the
426 excess of the compounds maximally. HeLa cells were then challenged with these samples
427 and incubated for 9 h to allow for a one-cycle infection. RV-A2 positive cells were determined
428 by fluorescence-activated cell sorting (FACS), using the intracellularly produced VP2 as a
429 readout. Fig. 3e demonstrates a concentration-dependent decrease in the number of cells
430 containing replicating RV-A2 upon pretreatment with PDS. Notably, a significant reduction

431 was also observed with 5 μ M of Phen-DC3. This result further strengthened our hypothesis
432 that PDS triggers a structural change in the encapsidated RNA as postulated from the
433 PaSTRY analysis, preventing its orderly egress from the capsid under *in vivo* conditions.

434 **PDS affects the conformation of the free RV genome and reduces viral infectivity in**
435 **the presence of Na⁺ but not in the presence of K⁺.**

436 We next embarked on an ultrastructural analysis of gently extracted rhinoviral RNA
437 for directly visualising the proposed PDS-induced structural change. The protein shell of RV-
438 A2 was proteolytically removed with proteinase K. To additionally examine a possible
439 differential impact of the prevalent extracellular (Na⁺) and intracellular (K⁺) monovalent
440 cation, the digestion was performed with the purified virus in sodium- as well as in
441 potassium-only containing phosphate buffer.

442 Initially, we evaluated the released naked (ex virion) viral RNA for the presence of
443 GQs by mixing with ThT. Importantly, due to its moderate affinity, ThT binds only to already
444 established GQs⁵⁶. At 30 °C, this resulted in a significant increase in the fluorescent signal
445 compared to the background (Fig 4a, upper panel). However, the formation of some GQs in
446 the viral RNA might be at least partially prevented by sequestration of the G-rich regions into
447 kinetically trapped competing structures. In order to assess this possibility quantitatively, we
448 heated the ex virion RNA for 10 min to 60 °C (the temperature where it unwinds to escape
449 from the RV-A2 capsid⁷³) in the presence of ThT followed by its slow refolding at room
450 temperature, thereby promoting the formation of the thermodynamically most stable
451 secondary structures. Under these conditions, the fluorescent emission intensity of the light-
452 up probe substantially raised by about 20-fold in both samples (Figure 4a, lower panel). This
453 indicated that distinctly more GQs were now available for ThT binding, likely resulting from a
454 conformational transition of kinetically trapped, metastable alternative (e.g. hairpin) structures
455 to the more stable quadruplex structure triggered by the elevated temperature. A similar
456 result was recently obtained in a study examining the kinetic vs thermodynamic control of a
457 sequence within an mRNA able to switch from a hairpin to a GQ, using N-methyl
458 mesoporphyrin (NMM) as light-up indicator⁸¹. The recorded ThT signal was consistently
459 higher for the Na⁺ compared to the K⁺-containing samples, despite the greater GQ stabilising
460 propensity of the latter cation, amounting to a ~40 % difference at 30 °C, which diminished to
461 just 9 % for the 60 °C heated samples. It suggests that the viral RNA molecule with intact 3D
462 structure is possibly more compact in the presence of the charge-neutralising K⁺, leading to
463 reduced accessibility of the already existing GQs for the ThT probe. Binding of ThT to GQs
464 forming during refolding of the heated viral RNA was expectedly much less affected by the
465 monovalent cation type when the probe was already present before full compaction of the
466 nucleic acid molecule.

467 We next incubated the ex virion RNA with 20 μ M PDS, again in a Na^+ or K^+ -containing
468 phosphate buffer, and submitted it to rotary shadowing. The platinum replicas were then
469 observed by transmission electron microscopy (TEM) (Fig. 4b). In the absence of PDS, the
470 ex virion RNA remained compact and approximately spherical though slightly deformed in
471 Na^+ (insets), indicating that compacting Mg^{2+} ⁸² and polyamines bound to the encapsidated
472 genome ^{83, 84} were not removed by our extraction procedure. A PaSTRy analysis with these
473 samples demonstrates the maintenance of a tertiary structure organisation under these
474 conditions (see below). Strikingly and entirely in line with the proposed pyridostatin-induced
475 RNA reorganisation deduced from the PaSTRy experiment (performed in PBS), PDS in the
476 Na^+ -containing buffer led to substantial elongation of these RNA cores, making them appear
477 irregular rods (left panel). Unexpectedly, no such effect of PDS was seen in the K^+ -containing
478 buffer, where the RNA remained roughly spherical (right panel).

479 We then employed atomic force microscopy (AFM) imaging to independently confirm
480 the TEM analysis outcome. AFM scans of identically prepared samples indeed yielded very
481 similar images (Fig. 4c and Supplementary Fig. S7). They show mostly irregular rods in Na^+ -
482 containing buffer + PDS with lengths of up to 200 nm and a diameter of about 10 nm
483 (Supplementary Fig. S7, upper panels) and spherical RNA in K^+ -containing buffer + PDS with
484 a diameter of roughly 25 nm (lower panels), compatible with the dimension of the capsid
485 internal cavity. This confirms that the structures shown in Fig. 4b are specific for the viral
486 RNA and not artefacts of the platinum contrasting and/or the drying process.

487 The drastic shape change only observed in Na^+ containing buffer likely results from
488 the rescuing of unstable GQs and/or the shifting of long-lived metastable structures with
489 alternative G-quartet forming ability to the more stable GQ conformation by PDS. This
490 presumably disturbs short and long-range interactions determining the global structure of the
491 RNA genome ^{85, 86}, similarly as described for certain small molecules on binding to tRNA and
492 riboswitches ^{87, 88}. Possibly, K^+ binding pockets in the viral RNA as e.g. found in ribosomal
493 RNA ⁸⁹ further constrain and condense its native tertiary structure compared to Na^+ , limiting
494 the access of the compound to these regions to account for the observed different effect of
495 PDS. To substantiate this hypothesis, we assessed the stability of the protein-free (ex virion)
496 RNA by carrying out a differential scanning fluorimetry (DSF) similarly as described by
497 Silvers, Keller ⁹⁰. Inspection of the DSF traces obtained in Na^+ and K^+ buffer indicated
498 similarly low accessibility of the viral RNA for SYTO 82 at 25 $^{\circ}\text{C}$ up to about 40 $^{\circ}\text{C}$, attesting
499 that the RNA molecule stays compact and extensively folded within this temperature range
500 (Supplementary Fig. S8). Here, SYTO 82 intercalates mostly into solvent-accessible double-
501 stranded regions located at the periphery, which seems less affected by choice of these
502 cations compared to the accessibility of GQs for ThT under similar conditions (Fig. 4). The
503 subsequent relatively rapid fluorescence increase from the lower baseline (at 44.5 $^{\circ}\text{C}$ and 51

504 °C for Na⁺ and K⁺, respectively) to the upper base line (= maximal response; at 54.3 °C and
 505 57.1 °C for Na⁺ and K⁺, respectively) relates to the disruption of (mostly) the RNA tertiary
 506 structure, now allowing SYTO 82 binding also to internally localised stem regions. The rise
 507 was ~2-fold (Na⁺) and ~1.2-fold (K⁺), indicating a more extensive unfolding in the sodium-
 508 containing buffer. The higher stability of the tertiary contacts of the viral genome in the
 509 presence of K⁺ is illustrated by the around 4 °C higher T_{m1}. The following progressive drop in
 510 emission intensity is due to melting of the more stable secondary structures with the release
 511 of SYTO 82, resulting in somewhat closer spaced higher melting temperatures T_{m2} (60.5 °C
 512 for Na⁺ and 63 °C for K⁺) for this transition.

513 The above *in vitro* data derived with the ex virion RNA altogether implies that its
 514 distinctly more compact tertiary structure imposed by K⁺ hinders the PDS molecules from
 515 arriving at internal regions able to transform into GQs on the binding of this compound. If
 516 correct, this should materialise in a distinctly smaller number of PDS molecules associated
 517 with the RV-A2 genome in potassium compared to sodium buffer. As assessing this figure is
 518 technically less demanding with encapsidated RNA, we quantified the amount of PDS that
 519 remained associated with the virions after incubation (20 µM) at 4 °C or at 34 °C for 4 h in
 520 Na⁺ or K⁺ containing buffers and subsequent extensive washing to remove any externally
 521 deposited traces of the compound. Table 3 shows that the number of PDS molecules, which
 522 penetrated the capsid upon incubation at 34 °C in Na⁺-containing buffer was by far higher
 523 than in all the other incubation conditions.

524

Treatment	PDS bound (moles/mole virus)	Relative to maximum
34 °C / Na ⁺	10	100 %
4 °C / Na ⁺	0.9	8.8 %
34 °C / K ⁺	0.2	1.4 %
4 °C / K ⁺	0.4	3.7 %

525

526 Table 3 – Mass spectrometry quantification of PDS content per virion.

527

528 The result further corroborated our hypothesis that K⁺, while commonly cooperating
 529 with PDS in GQ stabilisation⁹¹, unexpectedly protects the rhinoviral RNA from binding of this
 530 compound not only ex virion but also inside authentic viral particles (in virion). The magnitude
 531 of the difference of virion-incorporated PDS was quite impressive, as the encased
 532 polynucleotide of picornaviruses is already very compact^{92, 93}. This might have conceivably
 533 mitigated the tertiary structure changes in the presence of Na⁺ vs K⁺, believed to govern the
 534 extent of pyridostatin binding to viral QGRS when free in solution. A monovalent cation-
 535 dependent breathing activity as an additional source for that difference was ruled out by a

536 nanoDSF analysis of purified virions diluted in 100 mM sodium or potassium phosphate
537 buffer (Supplementary Fig. S9).

538 We then assessed whether the different PDS uptake by RV-A2 as found by MS
539 resulted in consequences on its infectivity by determining the TCID₅₀ of virus exposed to the
540 compound diluted in the respective monovalent cation-containing phosphate buffer. To avoid
541 any unspecific loss of infectivity due to thermal inactivation, we reduced the incubation
542 temperature to 25 °C and compensated for the resulting diminished breathing by extending
543 the treatment time to 20 h. As shown in Fig. 4d, the virus sample treated with PDS in the
544 presence of Na⁺ exhibited a titer reduction by 2 logs compared to control conditions (the
545 same buffer without PDS). By contrast, PDS treatment in K⁺ buffer did not affect the virus
546 titer as expected from the small amount of the compound detected by MS in the virion of
547 similarly treated virus (Table 3). Note that the slight reduction of infectivity on changing the
548 internal monovalent cation environment from Na⁺ to K⁺ in the absence of the PDS was not
549 significant.

550 Finally, we explored at what step of the infection cycle PDS might act on RV-A2 *in*
551 *vivo* (i.e. without pre-incubation) by a time-of-addition experiment. The virus was bound to
552 the cells for 30 min at 4 °C, PDS was added, and the cells shifted to 34 °C (T0). The same
553 experiment was conducted in parallel, except that PDS was added at T180 and T300,
554 respectively. This roughly corresponds to RV entry and uncoating (T0), RNA synthesis
555 (T180), and assembly (T300)^{94, 95, 96}. The cells were maintained for 9 h pi (one full cycle of
556 infection), and viral synthesis was measured by fluorescence-activated cell sorting (FACS).
557 As can be seen in Fig. 4e, the infection rate and viral synthesis was only significantly
558 impacted upon the addition of PDS at T0.

559 **DISCUSSION**

560 GQs have recently become a focal point as promising antiviral targets¹⁸. Despite this
561 surge in interest, the possible importance of this unconventional secondary structure remains
562 unexplored in picornaviruses. In this report, we fill this gap by focusing on RVs of the genus
563 *Enteroviruses* within the *Picornaviridae* family, which are responsible for more than 50 % of
564 common cold cases⁴. Using QGRS mapper³⁵, we identified putative intramolecular QGRS
565 for all completely sequenced rhinoviruses of clade A, B, and C. Altogether, RVs comprised
566 between 6 and up to 23 such QGRS motifs, which, with the exceptions of RV-A41 and RV-
567 B4, would give rise to only two-layer GQs. In most genomes, a variable fraction of the
568 predicted GQs would furthermore lack one G-quartet connecting loop. Most of the putative
569 QGRS are not or just weakly conserved, making it unlikely that they play an important role in
570 the virus life cycle. Nonetheless, four of these putative QGRS, all located in the ORF and
571 predicted to fold into conventional two-layer GQs, are highly conserved across all A, B and C

572 types (Fig. 1a); they were also identified in an independent analysis of all human virus
573 families by Lavzzo *et al.* ³⁴ using a proprietary software. While suggesting a functional
574 relevance for these QGRS, they might instead encode a critical sequence in the
575 corresponding polyprotein as an alternative reason for their strict maintenance, which
576 remains to be investigated. Atypical RNA GQs such as those with a bulged out nucleotide or
577 a vacancy will escape our analysis, but there are currently only a few reports on their
578 existence and possible role ⁴⁸.

579 The bioinformatics analysis indicated that targeting of GQs might be a promising new
580 approach for combating RV infections, with the strongly conserved GQs conceivably
581 presenting a high genetic barrier to drug resistance. For this purpose, we chose RV-A2 as
582 one of the best-characterised representative ⁹⁷. The 11 putative QGRS within its genomic
583 sequence would all give rise to just two-layer G-quartets (Supplementary Fig. S1). Using
584 various orthogonal biophysical assays, we demonstrated that the synthetic
585 ribooligonucleotides G11 and G20, representing the QGRS with the lowest and highest G-
586 score, respectively, formed all-parallel GQs in the presence of mM concentrations of K⁺ as
587 well as of Na⁺. This is also the most common conformation of naturally occurring RNA GQs
588 ⁹⁸. However, in contrast to many other examples ³⁶, their thermal stability was only
589 moderately (by ~4 to 5 °C) enhanced by K⁺ vs Na⁺. Also, G11 and G20 differed only little in
590 their stability with respect to the same coordinating alkaline cation, despite the considerably
591 higher G-score of G20. At lower temperatures (0 to 25 °C), a fraction of each
592 ribooligonucleotide folds into an A-type RNA structure (presumably hairpins). These
593 alternative conformers were not further explored as they were unstable at 34 °C, the optimal
594 temperature for RV-A2 replication ⁹⁹. This analysis is, to our knowledge, now the second
595 showing that an unconventional, two-layer zero-nucleotide loop RNA GQ as represented by
596 G11 is stable at physiological conditions. Interestingly, while no first loop was present in the
597 example of the previous report ³⁷, G11 lacks the third loop.

598 The ¹H-NMR analysis evidenced that both, G11 and G20, bound the GQ stabiliser
599 pyridostatin (PDS; ^{91, 100}). In all experiments with this compound, we specifically avoided Tris-
600 buffer as a solvent since we recently found it to promote aggregation of PDS into variably-
601 sized fibres ⁷¹. Using phosphate buffer instead, we noted the formation of PDS dimers, which
602 were the dominant species at concentrations ≥ 200 μM. Molecular docking indicated that this
603 association was largely driven by a π-π stacking interaction between two PDS molecules. An
604 *in silico* modelling with the structurally well-characterised pseudorabies virus RNA-derived
605 two-quartet GQ molecule PQS18-1 showed that both monomeric and dimeric PDS bind to
606 the exposed G-tetrad on the top or bottom of a GQ and share a second binding mode
607 involving the bases in the groove and a loop. (Supplementary Fig. S4). This is entirely in line
608 with a ¹⁹F-NMR study at a similar ligand (PDS) to RNA ratio ¹⁰¹ as used by us, which besides

609 π - π end-stacking, indicated additional (uncharacterised) binding site(s) for PDS on the
610 employed RNA GQ. Our analysis corroborates and extends previous reports on modelling
611 the GQ-PDS interaction, which proposes either a π - π end-stacking mode^{102, 103} or an
612 exclusive binding of PDS to the loop/groove interface¹⁰⁴, being furthermore restricted to
613 docking of just the monomeric compound. While our findings for PDS are novel, they are not
614 entirely unexpected, as stacking-mediated dimerisation and further aggregation of flat
615 polycyclic aromatic nucleic-acid binding dyes are already known for long (e.g. Bradley and
616 Wolf¹⁰⁵). Further, at least one other GQ-ligand (DMSB, a cyanine dye) was shown to bind as
617 a dimeric associate to the terminal G-tetrad and the groove of a DNA GQ¹⁰⁶.

618 Prompted by the evident GQ forming ability of two predicted putative QGRS
619 sequences in the RV-A2 genome, we exploited the virus breathing phenomenon to
620 investigate the impact of PDS on an encapsidated RNA. We found that infection of cells with
621 RV-A2 loaded with PDS in PBS buffer, which is rich in sodium and low in potassium, resulted
622 in substantial accumulation of subviral A- (or 135S) particles at 30 min pi, whereas most
623 native virus particles of the untreated control have already converted into empty B-particles.
624 This result strongly indicated that PDS compromised the uncoating of the viral genome.
625 Since PhenDC3, a chemically different GQ-interacting compound¹⁰⁷, had the same effect,
626 the targets were in all likelihood putative QGRS sequences in the genomic RNA that already
627 formed GQs within the capsid or could fold into such GQs on stabilisation by these
628 compounds. A PaSTRY analysis furthermore showed a markedly enhanced capsid mobility
629 of PDS-loaded virions compared to the untreated control. This strikingly resembled the
630 results of a low-level covalent modification of the encapsidated RNA of flock house virus
631 (FHV), a small icosahedral (+)ssRNA virus, by an aziridine derivative, which also led to
632 enhanced capsid mobility, suggested to originate from disrupted capsid protein-RNA
633 interactions in the native particle¹⁰⁸. By analogy, we concluded that PDS similarly triggered a
634 rearrangement of the encapsidated rhinoviral RNA affecting contacts with the inner surface
635 of the shell⁵, including those mediated by the recently identified enterovirus packaging
636 signals¹⁰⁹, leading to enhanced capsid breathing.

637 The proposed conformational change induced by PDS was directly verified by
638 ultrastructural analysis of rhinoviral RNA gently freed from the surrounding capsid by
639 proteinase K digestion. Instead of PBS, the incubation was done in a phosphate buffer
640 containing exclusively Na⁺ or K⁺ as the major extra- and intracellular monovalent cation to
641 assess their potential role. Remarkably, the GQ-specific light-up probe ThT revealed that in
642 both conditions, only a few GQs were already established in the ex virion RNA. Most putative
643 QGRS were apparently sequestered into alternative, long-lived (kinetically trapped),
644 metastable secondary structures, which transformed into thermodynamically more stable
645 GQs on heating and slow cooling of the viral RNA, resulting in the observed massively

646 increased ThT fluorescence emission. Presumably, during positive-strand RNA synthesis in
647 the infected cells, sequences of the nascent (+) strand comprising these QGRS fold much
648 faster into alternative, metastable conformations such as RNA hairpins than into the more
649 stable GQ (tens of microseconds vs hundreds of milliseconds^{110,111}) as soon as they emerge
650 from the active centre of the viral RNA replicase. If separated from each other by an
651 appreciable activation energy barrier, as indicated by the ThT analysis, these metastable
652 structures, following their rapid encapsidation (which is tightly coupled with replication¹¹²),
653 will persist in the progeny virions. The kinetically favoured formation of a metastable hairpin-
654 like structure instead of an alternative, more stable, GQ during co-transcriptional folding of a
655 nascent mRNA has been recently reported⁸¹.

656 Rotary shadowing and AFM demonstrated a profound PDS-induced shape change of
657 the ex virion RNA, in full agreement with our prediction. However, to our surprise, this
658 occurred only in the presence of Na⁺ but not the typically more strongly GQ-stabilising K⁺.
659 Then, the DSF analysis provided a plausible explanation for this initially puzzling
660 phenomenon, showing that potassium ions considerably strengthened the tertiary structure
661 of the ex virion RNA compared to sodium ions. We speculate that this is due to specific
662 chelation sites for K⁺ in the RV-A2 genomic RNA as described in certain ribozymes^{113,114}
663 and ribosomal RNA⁸⁹, which reinforce their tertiary structure. The viral RNA will likewise
664 further compact and rigidify when the postulated pockets are occupied by K⁺, which we
665 believe renders internally located, potential GQ-forming sequences inaccessible for
666 pyridostatin. In support of this, Favre and coworkers have previously shown that tight folding
667 of various RNA species substantially restricted the intercalation of ethidium bromide¹¹⁵.

668 Conversely, these GQ-forming sequences must remain accessible for PDS in the less
669 tightly packed ex virion RNA exposed to Na⁺ (at the same concentration as K⁺) to explain the
670 observed drastic structural reorganisation, which we attribute to the transition of QGRS
671 sequestered in the alternative, metastable conformations into GQs promoted by PDS. Apart
672 from its GQ-stabilising effect, this compound likely accelerates the process by its direct
673 participation in the GQ folding, thereby lowering its activation energy, as shown in an optical
674 tweezer study⁶¹. An analogous refolding of stem-loop structures into GQs induced by the G-
675 quadruplex ligand PDP (a PDS derivative) was recently proposed for an RNA of hepatitis C
676 virus¹¹⁶, and a profound effect on RNA long-range folding due to extensive differences in
677 secondary structures acquired with GQ formation was predicted in a bioinformatics analysis
678⁹¹. The unexpected “protective” effect of K⁺ was also clearly evident when RV-A2 was
679 incubated with PDS at breathing conditions, which did not result in a change in infectivity,
680 while the virus titer dropped by two logs on its replacement by Na⁺ in the buffer. Accordingly,
681 mass spectrometry revealed a marked accumulation of PDS inside the capsid only in the
682 presence of sodium and not potassium. It must be emphasised that the mere exchange of

683 Na⁺ for K⁺ in the capsid did not significantly impact the infectivity despite the different level of
684 compactness of the genomic RNA believed to regulate the compound access.

685 How may the binding of PDS to the QGRS of the viral genome under permissive
686 monovalent cation conditions affect its release from the capsid? In the currently favoured
687 model of enterovirus endosomal uncoating, the viral RNA must transiently unfold in order to
688 pass with its 3' end first through one of the in total 30 small pores (~1.5 nm diameter ⁷)
689 opening permanently at each of the two-fold icosahedral symmetry axis of the subviral A-
690 particle. The emerging RNA reaches the cytosol without contact with the endosomal contents
691 by passing through a connecting channel in the endosomal lipid bilayer formed by 5–6 copies
692 of expelled VP4 with a lumen diameter of between approximately 4.6 nm and 12 nm. Based
693 on preliminary data, host factor(s), in coordination with released VP4 acting as chaperone,
694 may pull the genome from the capsid once its unstructured poly(A) tract at the 3' end
695 appears outside of the endosome ^{5, 7, 64, 65, 66, 117, 118}. The forced transfer through the narrow
696 capsid opening will result in the reversible unzipping of secondary and tertiary structure
697 elements akin to the electrophoretically driven transport of structured RNA through the α -
698 hemolysin nanopore ¹¹⁹. The average number of PDS molecules (10) incorporated into the
699 capsid of RV-A2 in the presence of Na⁺ is comparable to the number of putative QGRS (11).
700 Assuming that they become folded into GQs as described for the ex virion RNA, it is tempting
701 to speculate that the stabilising effect of PDS prevents their unwinding by the above
702 mechanism. With an effective size of ~2.4 nm, the GQ-compound complex would sterically
703 block the ejection of the genomic RNA through the 2-fold related pore. This scenario closely
704 resembles the one suggested for compound-stabilised GQs located in the ORF of mRNAs on
705 encountering a translating ribosome, believed to plug its entry site featuring a diameter of
706 ~1.5 nm ¹²⁰, thereby obstructing further entry of the mRNA. However, though attractive, we
707 consider this rather unlikely, as our PaSTRY experiment with RV-A2 showed that
708 incorporation of PDS did not increase the temperature T_{max} , where RNA release starts
709 (Supplementary Fig. 6). This implies that PDS-binding by rhinoviral GQs did not raise their
710 stability above the one attributable to the most stable non-GQ secondary structure(s) formed
711 in the encapsidated rhinoviral RNA. We consequently favour an alternative mode of action
712 based on the likely structural reorganisation of the encapsidated genome triggered by PDS,
713 as indicated by PaSTRY and directly visualised with the ex virion RNA. This might
714 conceivably compromise the formation of the well-ordered RNA layer beneath the protein
715 shell of the A particle proposed to guide its ordered egress ⁵. In addition or alternatively, it
716 could dislodge the viral RNA's 3' end found to exit first ⁶⁵ from a position believed to reside in
717 the vicinity of one of the pores opening at the two-fold axis to allow its facile ejection, perhaps
718 directed by electrostatic focusing ¹²¹. Its PDS-driven relocation would result in a high entropic
719 penalty for finding such holes via thermal fluctuation (e.g. Polson and McLure ¹²²), critically

720 diminishing the successful vectorial traversal of the viral RNA through the capsid. This
721 problem is presently little appreciated, though one report already highlighted its role in a
722 coarse-grained model of RV-A2 uncoating ¹²³, and the results with PDS now provide first
723 experimental cues that it might matter. Worth mentioning, the icosahedral (+) ssRNA phages
724 MS2 has remarkably solved this problem by the strong binding of a hairpin at the 3' end of
725 the viral genome to a single copy of a maturation protein, which is directly incorporated into
726 the capsid, replacing a coat protein dimer at one of the icosahedral two-fold axes, being
727 pulled out alongside the RNA by attachment to and subsequent retraction of a bacterial F-
728 pilus ¹²⁴. Our reasoning does not contradict the fact that the heat-triggered uncoating of RV-
729 A2 is unaffected by PDS, as the substantially increased thermal motion will restore the
730 RNA's chances of finding a suitable exit pore. We note that several other RNA-binding
731 compounds incorporated into the encapsidated genomic RNA of rhino- and other
732 enteroviruses, such as RiboGreen, SYTO 82, neutral red, proflavine, and acridine orange did
733 not markedly affect their infectivity (the latter three when examined in the dark as they render
734 viruses photosensitive) ^{66, 69, 125, 126}. These molecules intercalate into double-stranded
735 secondary structures (up to 200 molecules for proflavine ¹²⁶ or about 1 per 23 nucleotides,
736 assuming 60 % of the ~7,500 nucleotides long encapsidated RNA being involved in
737 secondary structures as found for the related encephalomyocarditis virus ⁷⁵). While this leads
738 to partial unwinding of dsRNA segments, it apparently had little impact on the uncoating of
739 the viral RNA (e.g. Danthi, Tosteson ¹²⁷), which is not entirely surprising, given the different
740 interaction of GQ-stabilisers with their RNA target. An alternative model of enterovirus
741 uncoating proposes the dissociation of pentamers from the capsid at low pH, enabling exit of
742 the viral RNA as a bulk without the need for transient unfolding ^{11, 128}. The proposed
743 mechanism invokes protonation of bases of the RNA and dissociation of polyamines leading
744 to a close apposition of viral genome to positively charged regions of the capsid followed by
745 its cracking due to an increased pressure exerted on the capsid from the inside. This is
746 thought to lead to the expulsion of pentamer(s) followed by genome release. While PDS
747 might also interfere with such a process, we consider this mode of uncoating less important
748 for RV-A2, as cryo-EM analysis of low pH treated RV-A2 did not reveal the presence of
749 significant amounts of open particles ⁵.

750 Time-of-drug-addition showed that PDS had little consequence for RV-A2 protein
751 production when added after the uncoating stage. All subsequent events required for viral
752 reproduction occur in a high K⁺ and low Na⁺ cytosolic environment, limiting the access of the
753 viral RNA for the compound as found for the ex virion RNA. However, Lu and coworkers ¹²⁹
754 have recently shown that the enteroviral RNA within infected host cells is represented by an
755 ensemble of 3D structures, which substantially differed depend on the stage of engagement
756 (translation, replication) or when prevented from being packaged. It is, therefore, reasonable

757 to assume that even at the high intracellular K^+ level, in certain more open conformations of
758 these ensembles, the QGRS will become accessible for the compound, likely leading to
759 stabilisation of the respective GQs. A complete block of PDS binding by intracellular K^+ is
760 also unlikely based on recent life cell imaging of RNA GQ in the absence or presence of a
761 variant of PDS¹³⁰. Previous experiments with GQs featuring \geq four G-tetrad structures showed that
762 they could be unwound by the DHX36 helicase even when bound by GQ-stabilising ligands
763 such as PDS and PhenDC3, with a rate dependent on the thermal stability of the GQ-
764 compound complex¹³¹. We thus believe that the battery of intracellular host cell-derived
765 helicases¹³² together with the virus-encoded helicase 2C¹³³ efficiently disrupt any
766 intracellularly formed, intrinsically weak two-layer rhinoviral GQ even when bound by PDS.

767 In summary, we have shown that targeting QGRS by GQ-stabilising compounds
768 specifically inhibits the uncoating of a common cold virus and provides a mechanistic
769 explanation based on biophysical and ultrastructural analysis. Strikingly, PDS-uptake into the
770 virus occurs in the presence of physiological concentrations of Na^+ but not K^+ due to their
771 differential impact on viral RNA compaction rather than GQ formation. Finally, apart from its
772 potential as a new anti-rhinoviral compound, PDS did not interfere with the binding of RV-A2
773 to the host cell and likely preserved the immunogenic epitopes, making these low-infectious
774 particles attractive candidates in the development of attenuated vaccines for this group of
775 viruses.

776

777 **MATERIALS AND METHODS**

778 **Bioinformatic analysis of rhinoviral genomes for identification of putative GQs**

779 The QGRS mapping software was kindly made available by Paramjeet S. Bagga from
780 Ramapo College, New Jersey. The QGRS Mapper algorithm³⁵ predicts the ability of a
781 sequence containing G-repeats to fold into one to several distinct intramolecular
782 quadruplexes (termed Quadruplex-forming G-rich Sequences, QGRS) and assigns them a
783 stability score (G-score) based on published biophysical data. We performed our search
784 using the preset (default) search options: maximal length of 45, minimum G-group as 2 and
785 loop size from 0 to 36; allowing a loop size of 0 (zero loop) included non-canonical QGRS as
786 reported in yeast microsatellite DNA and mRNA involved in polyamine biosynthesis^{37, 134}.
787 The complete RV A (75), B (26) and C (19) sequences (120 sequences in total, available at
788 the time of writing and accessible through The Pirbright Institute) were used. The
789 corresponding GenBank accession numbers are listed in the Supplementary Table 1. Non-
790 overlapping sequences with a G-score \geq 10 within the sliding window were rendered as a
791 2D-line plot presenting the QGRS length and a heat-map showing the individual G-scores.

792 **Oligonucleotides and reagents**

793 Synthetic 27-mer RNA oligonucleotides (the positive control = human telomeric
794 repeat-containing RNA miniTERRA¹³⁵), G20, and G11 (for sequences see Table 1) and the
795 negative control (G20 with all Gs replaced by Cs), real-time PCR primers (RV-A2 Fw: 5'
796 gccccatgtgtgcagagtttc 3'; Rv: 5' aggtgtcagtggtatttattggtactaggctg 3' and Aichi virus A (AiV)
797 Fw: 5' tgtacaacaccactccatgtg 3'; Rv: 5' tccacagagagggagttcctg 3') were purchased from
798 Microsynth. Protein molecular weight markers, DNA ladder, ethidium bromide, Dulbecco's
799 Modified Eagle's Medium (DMEM), trypsin-EDTA solution, Pen-Strep antibiotics, bovine
800 serum albumin (BSA), thioflavin T (250 µM stock solution prepared in ultra-pure water and
801 kept at 4 °C), pyridostatin (4-(2-Aminoethoxy)-N2,N6-bis[4-(2-aminoethoxy)-2-quinoliny]-2,6-
802 pyridinedicarboxamide trifluoroacetate salt) (20 mM stock solution prepared in ultra-pure
803 water, aliquoted and kept at – 80 °C and thawed immediately before use), and Phen-DC3
804 (3,3'-[1,10-Phenanthroline-2,9-diylbis(carbonylimino)]bis[1-methylquinolinium] 1,1,1-
805 trifluoromethanesulfonate (1:2)) (1 mM stock solution prepared in DMSO, aliquoted and kept
806 at – 80 °C and thawed immediately before use) were purchased from Merck. TRIzol reagent,
807 SYTO 82 orange, Hoechst 33342 solution, and goat anti-mouse AlexaFluor 488, goat anti-
808 mouse IgG HRP-conjugated secondary antibody, and SuperSignal West Pico
809 chemiluminescent substrate were purchased from Thermo Fisher. Foetal bovine serum
810 (FBS) was purchased from Life Technologies. IRDye 680RD Goat anti-Mouse IgG secondary
811 antibody was purchased from LI-COR.

812 **Cells and virus**

813 HeLa Ohio cells were originally obtained from ATCC and maintained in DMEM,
814 supplemented with 10 % FBS, 1 % penicillin and streptomycin. Cells were kept in a
815 humidified 5 % CO₂-containing atmosphere at 37 °C. In infection assays, the serum
816 concentration was reduced to 2 % FBS and cells incubated at 34 °C, the optimal growth
817 temperature of RV-A2. For virus infection, we used RV-A2, initially acquired from ATCC and
818 propagated and purified following the protocol detailed in⁹⁹.

819 **ThT assay for detection of GQ**

820 Ribooligonucleotides were diluted in 100 mM potassium or sodium phosphate buffer
821 (pH 7.4) to a final concentration of 5 µM, incubated for 10 min at 90 °C followed by 10 min at
822 4 °C, and mixed with ThT (final concentration 5 µM). Samples were excited at 440 nm, and
823 emission was measured at 490 nm using a PerkinElmer VICTOR Nivo Multimode Plate
824 Reader.

825 For examination of viral RNA, purified RV-A2 (~2 µg) was suspended in 100 mM
826 sodium phosphate buffer or 100 mM potassium phosphate buffer, both at pH 7.4, and the
827 protein shell was digested with 5 µg of proteinase K at 4 °C overnight. The following day, the

828 ex virion RNA samples were ultrafiltered using 100 K Merck Amicon Ultra Filter units
829 according to the manufacturer's protocol, followed by 4 X 400 µl washes with the respective
830 buffers. Samples were mixed with ThT (final concentration 5 µM), and the volume was
831 adjusted to 100 µl. The ThT fluorescence signal was acquired as described above. The
832 sample labelled at 30 °C was maintained at room temperature all the time. The 60 °C
833 labelled sample was incubated at this higher temperature for 10 min and cooled to room
834 temperature on the bench for 30 min, followed by the acquisition of the fluorescence signal.

835 **Fluorescent indicator Displacement assay (FiD)**

836 ThT-containing ribooligonucleotide samples prepared as above (100 µl) were
837 dispensed into wells of a 96-well plate. PDS was then added in 2 µM steps up to 50 µM, and
838 the respective fluorescence was recorded at 34 °C. Signal loss due to ThT dilution by the
839 solvent control (water) was negligible. A titration curve was constructed from three
840 independent experiments by plotting the percentage fluorescence drop (obtained by dividing
841 the mean fluorescence intensity at each PDS concentration by the mean initial signal ((no
842 PDS) x 100) against the concentration of PDS.

843 **Particle Stability Thermal Release Assay (PaSTRy)**

844 PaSTRy-related experiments were performed according to Real-Hohn, Groznica ⁷³
845 with minor adaptations. RNA exposure was monitored with SYTO 82 in a Bio-Rad CFX
846 Connect Real-Time PCR instrument. Purified RV-A2 (~3.5 µg) was pre-incubated ± PDS at
847 200 µM final concentration and with PBS (volume adjusted to 70 µl) at 4 °C (no virus
848 breathing) and 34 °C (permitting virus breathing) for 4 h. Unbound PDS was removed by
849 centrifugation in 100 K Merck Amicon Ultra Filter units according to the manufactures'
850 protocol, followed by 4 X 400 µl washes with PBS at 25 °C to eliminate any remaining
851 unbound PDS. SYTO 82 was added to a final concentration of 5 µM, and the volumes were
852 adjusted to 70 µl with PBS. Three 20 µl aliquots from each of these samples were dispensed
853 into the wells of a thin-walled PCR plate, and the temperature was ramped from 25 - 95 °C at
854 1.5 °C / min, and SYTO 82 light-up fluorescence was recorded. Six independent
855 measurements were done for each condition. Data were rendered as a dot plot revealing the
856 onset of access of SYTO 82 to the RNA (Real-Hohn, Groznica ⁷³ and Supplementary Fig.
857 S1).

858 **Differential Scanning Fluorimetry (DSF) analysis of RV-A2 ex virion RNA**

859 Purified RV-A2 (~2 µg) was suspended in 100 mM sodium phosphate buffer or 100
860 mM potassium phosphate buffer, both at pH 7.4, and the protein shell was digested with 5 µg
861 of proteinase K at 4 °C overnight. On the following day, the ex virion RNA samples were
862 ultrafiltered using 100 K Merck Amicon Ultra Filter units according to the manufactures'
863 protocol, followed by 4 X 400 µl washes with the respective buffers. SYTO 82 was added to a

864 final concentration of 5 μ M, and the volumes were adjusted to 70 μ l with the respective
865 buffers. Three 20 μ l aliquots from each of these samples were dispensed into the wells of a
866 thin-walled PCR plate, and the temperature was ramped from 25 - 95°C at 1.5 °C / min, and
867 SYTO 82 light-up fluorescence was recorded. Three independent measurements were
868 performed for each condition, and the fluorescence signal means for each condition were
869 displayed.

870 **Virus yield reduction assay**

871 Purified RV-A2 (~1 μ g) \pm PDS (20 μ M final concentration, or ultra-pure water as
872 control), was adjusted to 100 μ l in 100 mM sodium or potassium phosphate buffer (pH 7.4)
873 and incubated overnight at 25 °C. Unbound PDS was removed by centrifugal ultrafiltration as
874 above. The virus titers (TCID₅₀) were determined as described elsewhere¹³⁶.

875 **Immunocytochemistry and flow cytometry**

876 Cells grown in a 6-well plate until 90 % confluent were infected with 0.1 μ g RV-A2
877 either untreated (corresponding to an MOI of 1) or pretreated with PDS (at 20 or 200 μ M final
878 concentration) diluted in PBS and incubated for 4 h at 34 °C. The unbound PDS was
879 removed by centrifugal ultrafiltration. The same experiment was carried out with Phen-DC3
880 at 1 μ M and 5 μ M. At 9 h pi the infection medium was aspirated, cells were washed once with
881 PBS and detached with 0.1 % trypsin in 0.05 % EDTA. The trypsin was inactivated with 10 %
882 FBS in DMEM. Cells were harvested by low-speed centrifugation at 300 g for 3 min at 4 °C.
883 The pellet was resuspended in 500 μ l ice-cold PBS, followed by the addition of 500 μ l 4 %
884 formaldehyde in PBS and incubation for 10 min at 4 °C. This and all subsequent steps were
885 done with gentle rocking. Cells were subsequently washed 3 times with 1 ml of ice-cold
886 PBST (PBS plus 0.1 % Tween-20, pH 7.4) at 4 °C, resuspended in PBS + 0.1 % Triton X-
887 100, and incubated for 10 min at 4 °C. The cells were then incubated in blocking buffer (1 %
888 BSA, 0.1 % Tween-20 PBS (pH 7.4)) for 30 min at 4 °C, followed by incubation with 10 μ g/ml
889 8F5, a monoclonal antibody specific for VP2 of RV-A2¹³⁷ in blocking buffer for 1 h at 4 °C.
890 Cells were again washed 3 times with PBST and incubated for 1 h with goat anti-mouse
891 AlexaFluor 488 antibody diluted (1 : 1,000) in blocking buffer at 4 °C. Samples were then
892 incubated with Hoechst dye solution in PBS (1 : 2,000) for 10 min for staining nuclei, followed
893 by 3 times washing with PBST. They were finally resuspended in PBS and analysed with a
894 BD Bioscience FACSAria III flow cytometer; more than 10⁴ events were acquired for each
895 sample. Forward scattering (FSC) vs VP2 (FITC-A) plots were generated by Tree Star
896 FlowJo X v10.0.7 software.

897 **Immunoprecipitation**

898 Cells grown in a 10 cm culture plate until ~80 % confluent were infected with ~1 μ g
899 RV-A2 pretreated \pm 200 μ M PDS (as for flow cytometry, see above) at 34 °C; 30 min pi the

900 medium was removed and replaced with 1 ml PBS. The cells were gently detached with a
901 cell scraper (Corning) and subjected to 3 freeze/thaw cycles. Cell debris was removed by
902 low-speed centrifugation, and the supernatant was divided into 2 aliquots. From one aliquot,
903 viral uncoating intermediates (i.e. subviral A- and B-particles) were immunoprecipitated using
904 MAb 2G2⁷⁷ bound to protein G magnetic beads (Dynabeads-Protein G; Life Technologies).
905 The second aliquot was taken as a negative control by omitting MAb 2G2 but otherwise
906 processing it identically. As a positive control, ~1 µg of heated RV-A2 (10 min at 56 °C
907 resulting in an almost ~100 % conversion into subviral B-particles) was processed identically.
908 After extensive washing in PBS, the immunoprecipitates were resuspended in 100 µl PBS.
909 Two µl of 5X protein sample buffer were added to 18 µl of each sample and the mixture
910 heated to 95 °C for 10 min. The proteins were separated by SDS-PAGE (10 %) followed by
911 transfer to an Immobilon-P membrane. The Western blot was done essentially as described
912 in¹³⁸. In brief, the viral protein (VP2) was detected with mouse monoclonal antibody (8F5),
913 anti-mouse-horseradish peroxidase and SuperSignal West Pico PLUS chemiluminescent
914 substrate (Thermo Fisher). The signal was quantified using a ChemiDoc Gel Imaging System
915 (Bio-Rad). To investigate the proportion of A- and B-particles, the viral RNA was also
916 quantified in 50 µl of the remaining respective resuspended immunoprecipitates. As internal
917 control and for normalisation, RNA obtained from 100 µl Aichi virus (AiV; a member of the
918 kobuvirus species of the *Picornaviridae* family), corresponding to 2×10^7 TCID₅₀, was added
919 to each sample. RNA was recovered by TRIzol (1 ml; Invitrogen) extraction and precipitation
920 (together with GlycoBlue from Invitrogen) following the manufacturer's protocol. First strand
921 cDNA synthesis was carried out with the NEBNext reagent kit (New England Biolabs, UK)
922 using random primers and the samples quantified by qPCR using primers specific for RV-A2
923 or AiV, using a CFX96 Touch Real-Time PCR Detection System (Bio-Rad).

924 **Sucrose gradient sedimentation**

925 Cells were infected with RV-A2 pretreated ± 200 µM PDS for 30 min at 34 °C as
926 described above (immunoprecipitation method), the medium was removed, and 1 ml PBS
927 was added, followed by gently dislodging the cells with a cell scraper (Corning). The
928 resuspended cells were subjected to 3 freeze/thaw cycles. Cell debris was removed by low-
929 speed centrifugation. Five hundred µl of the resulting supernatants containing the (sub)viral
930 particles were deposited onto preformed 10–40 % (w/v) sucrose density gradients made in
931 virus buffer (5 ml of 50 mM NaCl, 20 mM Tris-HCl, pH 7.4) and centrifuged at 4 °C for 30 min
932 in an SW55 Ti rotor (Beckman) at 286,794 g. Aliquots (250 µl) were collected from top to
933 bottom and frozen at –80 °C until further use. Twenty µl of each fraction were deposited onto
934 a methanol-activated Immobilon-P membrane (Millipore) placed in a 96-well Bio-Dot
935 Microfiltration Apparatus (Bio-Rad) for the dot blot analysis. Viral protein VP2 was detected
936 using the VP2-specific MAb 8F5 and IRDye 680RD Goat anti-mouse IgG secondary antibody

937 essentially as described for the development of the Western blot further above. The
938 fluorescent signal acquisition was performed in an Odyssey Infrared Imager (LI-COR).

939 **Time-of-drug addition experiment**

940 HeLa cells grown in 6-well tissue culture plates to roughly 80 % confluency were
941 challenged with RV-A2 at MOI = 10 for 30 min in infection medium at 4 °C with steady
942 rocking allowing the virus to attach to its receptor while preventing its internalisation for
943 achieving a synchronised infection. Then, the inoculum was removed, cells were washed
944 three times with PBS, a fresh infection medium was added, and incubation continued at 34
945 °C to trigger virus internalisation (T = 0 min pi). Immediately (T0) or after 60, 180 or 300
946 minutes (T60, T180 and T300 respectively), PDS was added to a final concentration of 20
947 µM. At 9 h pi, cells were processed for flow cytometry and immunocytochemistry as
948 described above. Using Tree Star FlowJo X v10.0.7 software, a FITC-A histogram showing
949 the mean fluorescence intensity (MFI) from more than 10⁴ events corresponding to *de novo*
950 produced VP2 was generated upon gating based on FSC and SSC properties.

951 **Nuclear magnetic resonance**

952 NMR experiments were performed with a 600 MHz Bruker Avance 3HD+spectrometer
953 at 4, 25 and 34 °C. The concentration of the ribooligonucleotides was ~0.25 mM. The
954 solution contained 10 mM sodium phosphate (pH 7.4), 100 mM KCl, and 10 % D₂O. ¹H NMR
955 shifts were referenced relative to (external) DSS (Sodium trimethylsilylpropanesulfonate).
956 The typical sample volume was 500 µl. Water suppression for ¹H NMR spectra was
957 performed using a double WATERGATE echo with extra water flip-back pulse to avoid
958 saturation of exchangeable hydrogens due to hydrogen exchange ¹³⁹. Typically ca 1000
959 scans each were required to obtain a ¹H NMR spectrum with sufficient signal to noise ratio.
960 For the hydrogen-deuterium exchange (DXH) assay, 0.3 mM G11 RNA was prepared in 10
961 mM sodium phosphate (pH 7.4), 100 mM KCl and diluted 1:3 in D₂O to 0.1 mM G11 RNA
962 (final concentration) immediately before acquisition. The signal attenuation of the imino
963 hydrogens due to hydrogen-deuterium exchange was observed in a series of ¹H NMR
964 spectra throughout 9 h.

965 **Circular Dichroism (CD) and melting profile**

966 Ribooligonucleotides were used at 20 µM in 100 mM potassium phosphate (pH 7.4)
967 or 100 mM sodium phosphate (pH 7.4), as indicated in the figure. Unfolding and refolding
968 experiments were performed with temperature ramping from 25 - 90 °C or 90 - 25 °C,
969 respectively, at 1 °C/min using a Chirascan plus spectropolarimeter equipped with a Peltier
970 temperature control system from Applied Photobiophysics. The buffer's CD spectrum was
971 recorded identically and subtracted from the spectrum obtained for the RNA-containing
972 solution. Data were zero-corrected at 400 nm.

973 **Ribooligonucleotide electrophoresis**

974 The synthetic ribooligonucleotides (miniTERRA, G11, and G20) in 20 µl 100 mM
975 potassium phosphate buffer (pH 7.4) at a final concentration of 25 µM were heated to 95 °C
976 for 10 min, transferred to 4 °C and incubated for an additional 10 min. Samples were then
977 mixed with Gel Loading Dye (Blue 6X; New England Biolabs) and loaded onto a non-
978 denaturing 12 % polyacrylamide gel containing 150 mM KCl. The gel was run in TBE buffer
979 supplemented with KCl at 150 mM. Electrophoresis was performed in a fume hood with the
980 chamber placed in an ice bucket for 3 h at 50 V. Ribooligonucleotides and DNA ladder (Low
981 Molecular Weight DNA Ladder, New England Biolabs) were stained by incubation for 30 min
982 in Gel-Red 3X solution and scanned in a Typhoon fluorescent scanner (General Electric,
983 USA).

984 **Electron Microscopy and Rotary Shadowing**

985 Purified RV-A2 (~2 µg) was suspended in 100 mM sodium phosphate buffer or 100
986 mM potassium phosphate buffer, both at pH 7.4, and the protein shell was digested with 5 µg
987 proteinase K at 4 °C overnight. The ex virion RV-A2 RNA was first diluted to a concentration
988 of approximately 0.1 mg/ml in the same buffers used for digestion and subsequently diluted
989 1:1 in spraying buffer, containing 200 mM ammonium acetate and 60 % (v/v) glycerol, pH
990 adjusted to 7.4. Immediately after dilution, the samples were sprayed onto freshly cleaved
991 mica chips (Agar Scientific, UK) and quickly transferred into a BAL-TEC MED020 high
992 vacuum evaporator (BAL-TEC, Liechtenstein) equipped with electron guns. While rotating,
993 samples were coated with 0.6 nm platinum (BAL TIC, Germany) at an angle of 7°, followed by
994 6 nm carbon (Balzers, Liechtenstein) at 90°. The obtained replicas were floated off from the
995 mica chips, picked up on 400 mesh Cu/Pd grids (Agar Scientific), and inspected in an FEI
996 Morgagni 268D TEM (Thermo Fisher Scientific, The Netherlands) operated at 80kV. Images
997 were acquired using an 11 megapixel Morada CCD camera (Olympus-SIS, Germany).

998 **Atomic force microscopy (AFM)**

999 AFM imaging of the ex virion RV-A2 genomic RNA was done as follows:
1000 approximately 2 µg of purified RV-A2 were suspended in 100 mM sodium phosphate buffer
1001 or 100 mM potassium phosphate buffer, and its protein shell was digested with 10 U of
1002 proteinase K at 4 °C overnight. The samples were incubated with 20 µM PDS for 10 min,
1003 then deposition onto freshly cleaved mica and immediately imaged in a Pico-SPM atomic
1004 force microscope (Molecular Imaging, Phoenix, AZ, USA) equipped with a fluidic cell. The
1005 AFM images were acquired with acoustic AC (Tapping) mode using the MSNL (Bruker)
1006 cantilever E (with the nominal spring constant of 0.1 N/m) at 15 kHz. The scanning speed
1007 was 3000 nm/s, and the number of pixels per line was 256.

1008 **Molecular docking procedure**

1009 The chemical structure for PDS in the monomer and dimer forms at pH = 7.4 was built
1010 and minimised in terms of energy by Density Functional Theory (DFT), with the Becke-3-Lee
1011 Yang Parr (B3LYP) method and standard 6-31G* basis set, available in Spartan'18 software
1012 (Wavefunction, Inc., Irvine, USA) [<https://www.wavefun.com/> accessed in January 2021]. The
1013 physicochemical properties, logP and dipolar moment, were also calculated using the energy
1014 parameters described above. The parallel RNA GQ's crystallographic structure was obtained
1015 from the Protein Data Bank (PDB) [<https://www.rcsb.org/> accessed in January 2021] with
1016 access code 6JJH⁴⁷. This structure was used as a 3D model for molecular docking
1017 calculations to gain insights into the mode(s) of interaction between GQ RNAs and PDS due
1018 to its structural similarity with the RNA GQs used in the experimental assays and its high
1019 crystallographic resolution to about 1.74 Å. The molecular docking calculations were
1020 performed using GOLD 5.7 software (Cambridge Crystallographic Data Centre, Cambridge,
1021 UK) [<https://www.ccdc.cam.ac.uk/solutions/csd-discovery/components/gold/> accessed in
1022 January 2021]. Hydrogen atoms were added to the RNA GQ structure according to ionisation
1023 and tautomeric states inferred by the software. For methodology validation, redocking studies
1024 with the heterocyclic porphyrin TMPyP4⁴⁷ were carried out to evaluate the best scoring
1025 function to be used in the *in silico* studies (ChemPLP, Goldscore, ChemScore or ASP). The
1026 root mean square deviation (RMSD) value was 1.0039, 1.1222, 1.1999, and 0.9305 Å for
1027 ChemPLP, Goldscore, ChemScore and ASP, respectively. Since the lowest RMSD value
1028 was obtained with ASP, this function was then used in all further *in silico* studies. For each
1029 search, a 10 Å radius spherical volume around the RNA GQ structure was selected. The best
1030 docking poses were identified through the best docking score value, and figures were
1031 generated with PyMOL Delano Scientific LLC software (Schrödinger, New York, USA)
1032 [<https://www.pymol.org/2/> accessed in December 2020].

1033 **Metabolomic analysis**

1034 Purified RV-A2 (12 µg) was incubated with PDS at 20 µM final concentration in 100
1035 mM potassium phosphate (pH 7.4) or 100 mM sodium phosphate (pH 7.4) for 4 h at 4 °C (no
1036 virus breathing) or 34 °C (permitting virus breathing). Unbound PDS was removed from virus
1037 samples by centrifugation in 100 K Merck Amicon Ultra Filter units according to the
1038 manufactures' protocol, followed by 4 X 400 µl washes with the respective buffers to
1039 eliminate any remaining unbound PDS. Subsequently, virus samples were incubated with
1040 acidified methanol (1 % formic acid) for denaturing the capsid to allow extraction of PDS
1041 captured inside the virion. After centrifugation, the supernatant was analysed with liquid
1042 chromatography-tandem mass spectrometry (LC-MS/MS). One µl of the extract was injected
1043 in an RSLC ultimate 3000 (Thermo Fisher Scientific) directly coupled to a TSQ Vantage
1044 mass spectrometer (Thermo Fisher Scientific) via electrospray ionisation in the positive ion

1045 mode. A Kinetex C18 column was used (100 Å, 150 x 2.1 mm) beforehand to separate PDS
1046 from other components of the extract, employing a flow rate of 80 µl/min. A 10-minute linear
1047 gradient was used from 95 % A (1 % acetonitrile, 0.1 % formic acid in water) to 80 % B (0.1
1048 % formic acid in acetonitrile). LC-MS/MS was performed by employing the selected reaction
1049 monitoring (SRM) mode of the instrument using the transitions 597.4 m/z → 511.3 m/z (CE
1050 20) and 597.4 m/z → 468.3 m/z (CE 25). Data were interpreted manually, and the absolute
1051 amount of PDS quantified with a calibration curve obtained with external pyridostatin
1052 standard solutions.

1053 **Quantification and statistical analysis**

1054 All experiments were done at least in duplicate for a total of $n \geq 2$ biological replicates.
1055 Data are displayed as mean \pm standard deviation (SD) (for $n > 2$). Statistical significance was
1056 determined using the unpaired one-tailed Student's t-test. The p-value and sample size n of
1057 each experimental group are provided in the respective figure legends.

1058 **ACKNOWLEDGEMENT**

1059 We express our gratitude to Irene Goesler for virus production and purification. Our
1060 special thanks go to Arthur Sedivy, Thomas Koecher and Marlene Brandstetter from the
1061 Vienna BioCenter Core Facilities (VBCF) for their valuable help and assistance. Mass
1062 spectrometry (Metabolomics Facility), electronic microscopy (Electron Microscopy Facility),
1063 and circular dichroism (Protein Technologies Facility) were performed at VBCF.

1064 **FUNDING**

1065 Funded by the Austrian Science Fund (FWF), projects P27444 and P31392 to DB
1066 and P27196 to HK.

1067 **CONFLICT OF INTEREST**

1068 The authors declare no conflict of interest.

1069 **AUTHOR CONTRIBUTION**

1070 AR-H, DB, and HK designed the study and wrote the manuscript. AR-H, MG, GK, RZ,
1071 OAC, and LV conducted experiments, analysed and interpreted the data. PH provided advice
1072 in the design of the experiments and analysis of the data. All authors contributed to the
1073 article and approved the submitted version.

1074 **DATA AVAILABILITY**

1075 All datasets presented in this study are included in the article/supplementary material.

1076 **REFERENCES**

- 1077 1. Kennedy JL, Pham S, Borish L. Rhinovirus and Asthma Exacerbations. *Immunol Allergy Clin North Am* **39**, 335-344 (2019).
1078
- 1079 2. Gern JE, Busse WW. Association of rhinovirus infections with asthma. *Clin Microbiol Rev* **12**,
1080 9-18 (1999).
1081
- 1082 3. Tang JW, *et al.* Global epidemiology of non-influenza RNA respiratory viruses: data gaps and
1083 a growing need for surveillance. *Lancet Infect Dis*, (2017).
1084
- 1085 4. Heikkinen T, Jarvinen A. The common cold. *Lancet* **361**, 51-59 (2003).
1086
- 1087 5. Pickl-Herk A, *et al.* Uncoating of common cold virus is preceded by RNA switching as
1088 determined by X-ray and cryo-EM analyses of the subviral A-particle. *Proc Natl Acad Sci U S A*
1089 **110**, 20063-20068 (2013).
1090
- 1091 6. Garriga D, *et al.* Insights into minor group rhinovirus uncoating: the X-ray structure of the
1092 HRV2 empty capsid. *Plos Pathog* **8**, e1002473 (2012).
1093
- 1094 7. Bostina M, Levy H, Filman DJ, Hogle JM. Poliovirus RNA is released from the capsid near a
1095 twofold symmetry axis. *J Virol* **85**, 776-783 (2011).
1096
- 1097 8. Shingler KL, *et al.* The enterovirus 71 A-particle forms a gateway to allow genome release: a
1098 cryoEM study of picornavirus uncoating. *Plos Pathog* **9**, e1003240 (2013).
1099
- 1100 9. Kumar M, Blaas D. Human rhinovirus subviral a particle binds to lipid membranes over a
1101 twofold axis of icosahedral symmetry. *J Virol* **87**, 11309-11312 (2013).
1102
- 1103 10. GropPELLI E, *et al.* Picornavirus RNA is protected from cleavage by ribonuclease during virion
1104 uncoating and transfer across cellular and model membranes. *Plos Pathog* **13**, e1006197
1105 (2017).
1106
- 1107 11. Buchta D, *et al.* Enterovirus particles expel capsid pentamers to enable genome release. *Nat*
1108 *Commun* **10**, 1138 (2019).
1109
- 1110 12. Hrebik D, *et al.* ICAM-1 induced rearrangements of capsid and genome prime rhinovirus 14
1111 for activation and uncoating. *Proc Natl Acad Sci U S A* **118**, (2021).
1112
- 1113 13. Royston L, Tapparel C. Rhinoviruses and Respiratory Enteroviruses: Not as Simple as ABC.
1114 *Viruses* **8**, 16 (2016).
1115
- 1116

- 1117 14. Lin JY, Chen TC, Weng KF, Chang SC, Chen LL, Shih SR. Viral and host proteins involved in
1118 picornavirus life cycle. *J Biomed Sci* **16**, 103 (2009).
- 1119
1120 15. Jiang P, Liu Y, Ma HC, Paul AV, Wimmer E. Picornavirus morphogenesis. *Microbiol Mol Biol*
1121 *Rev* **78**, 418-437 (2014).
- 1122
1123 16. Baggen J, Thibaut HJ, Strating J, van Kuppeveld FJM. The life cycle of non-polio enteroviruses
1124 and how to target it. *Nature reviews Microbiology* **16**, 368-381 (2018).
- 1125
1126 17. Berzal-Herranz A, Romero-López C, Berzal-Herranz B, Ramos-Lorente S. Potential of the
1127 Other Genetic Information Coded by the Viral RNA Genomes as Antiviral Target.
1128 *Pharmaceuticals* **12**, 38 (2019).
- 1129
1130 18. Ruggiero E, Richter SN. Viral G-quadruplexes: New frontiers in virus pathogenesis and
1131 antiviral therapy. *Annu Rep Med Chem* **54**, 101-131 (2020).
- 1132
1133 19. Xiao C-D, Shibata T, Yamamoto Y, Xu Y. An intramolecular antiparallel G-quadruplex formed
1134 by human telomere RNA. *Chemical Communications* **54**, 3944-3946 (2018).
- 1135
1136 20. Jeng SC, Chan HH, Booy EP, McKenna SA, Unrau PJ. Fluorophore ligand binding and complex
1137 stabilization of the RNA Mango and RNA Spinach aptamers. *Rna* **22**, 1884-1892 (2016).
- 1138
1139 21. Dolinnaya NG, Ogloblina AM, Yakubovskaya MG. Structure, properties, and biological
1140 relevance of the DNA and RNA G-quadruplexes: Overview 50 years after their discovery.
1141 *Biochemistry (Moscow)* **81**, 1602-1649 (2016).
- 1142
1143 22. Masai H, Tanaka T. G-quadruplex DNA and RNA: Their roles in regulation of DNA replication
1144 and other biological functions. *Biochemical and biophysical research communications* **531**,
1145 25-38 (2020).
- 1146
1147 23. Ishiguro A, Kimura N, Watanabe Y, Watanabe S, Ishihama A. TDP-43 binds and transports G-
1148 quadruplex-containing mRNAs into neurites for local translation. *Genes to cells : devoted to*
1149 *molecular & cellular mechanisms* **21**, 466-481 (2016).
- 1150
1151 24. Majee P, *et al.* Inhibition of Zika virus replication by G-quadruplex-binding ligands. *Mol Ther*
1152 *Nucleic Acids* **23**, 691-701 (2021).
- 1153
1154 25. Artusi S, *et al.* Antiviral Activity of the G-Quadruplex Ligand TMPyP4 against Herpes Simplex
1155 Virus-1. *Viruses* **13**, (2021).
- 1156
1157 26. Zhao C, *et al.* Targeting RNA G-Quadruplex in SARS-CoV-2: A Promising Therapeutic Target for
1158 COVID-19? *Angew Chem Int Ed Engl* **60**, 432-438 (2021).
- 1159

- 1160 27. Wang SR, *et al.* Chemical Targeting of a G-Quadruplex RNA in the Ebola Virus L Gene. *Cell*
1161 *Chem Biol* **23**, 1113-1122 (2016).
- 1162
1163 28. Tlučková K, *et al.* Human Papillomavirus G-Quadruplexes. *Biochemistry-Us* **52**, 7207-7216
1164 (2013).
- 1165
1166 29. Perrone R, Artusi S, Butovskaya E, Nadai M, Pannecouque C, Richter SN. G-Quadruplexes in
1167 the Human Immunodeficiency Virus-1 and Herpes Simplex Virus-1: New Targets for Antiviral
1168 Activity by Small Molecules. (ed[^](eds). Springer International Publishing (2015).
- 1169
1170 30. Brázda V, *et al.* G-quadruplexes in H1N1 influenza genomes. *BMC Genomics* **22**, 77 (2021).
- 1171
1172 31. Wang S-R, *et al.* A highly conserved G-rich consensus sequence in hepatitis C virus core gene
1173 represents a new anti-hepatitis C target. *Science Advances* **2**, e1501535 (2016).
- 1174
1175 32. Ruggiero E, Richter SN. G-quadruplexes and G-quadruplex ligands: targets and tools in
1176 antiviral therapy. *Nucleic Acids Res* **46**, 3270-3283 (2018).
- 1177
1178 33. Bezzi G, Piga EJ, Binolfi A, Armas P. CNBP Binds and Unfolds In Vitro G-Quadruplexes Formed
1179 in the SARS-CoV-2 Positive and Negative Genome Strands. *International Journal of Molecular*
1180 *Sciences* **22**, 2614 (2021).
- 1181
1182 34. Lavezzo E, *et al.* G-quadruplex forming sequences in the genome of all known human viruses:
1183 A comprehensive guide. *PLoS Comput Biol* **14**, e1006675 (2018).
- 1184
1185 35. Kikin O, D'Antonio L, Bagga PS. QGRS Mapper: a web-based server for predicting G-
1186 quadruplexes in nucleotide sequences. *Nucleic Acids Res* **34**, W676-682 (2006).
- 1187
1188 36. Joachimi A, Benz A, Hartig JS. A comparison of DNA and RNA quadruplex structures and
1189 stabilities. *Bioorg Med Chem* **17**, 6811-6815 (2009).
- 1190
1191 37. Lightfoot HL, Hagen T, Clery A, Allain FH, Hall J. Control of the polyamine biosynthesis
1192 pathway by G2-quadruplexes. *Elife* **7**, (2018).
- 1193
1194 38. Jodoin R, Bauer L, Garant JM, Mahdi Laaref A, Phaneuf F, Perreault JP. The folding of 5'-UTR
1195 human G-quadruplexes possessing a long central loop. *RNA* **20**, 1129-1141 (2014).
- 1196
1197 39. Bolduc F, Garant JM, Allard F, Perreault JP. Irregular G-quadruplexes Found in the
1198 Untranslated Regions of Human mRNAs Influence Translation. *J Biol Chem* **291**, 21751-21760
1199 (2016).
- 1200

- 1201 40. Ashraf S, Brockman-Schneider R, Bochkov YA, Pasic TR, Gern JE. Biological characteristics and
1202 propagation of human rhinovirus-C in differentiated sinus epithelial cells. *Virology* **436**, 143-
1203 149 (2013).
- 1204
1205 41. Rohll JB, Percy N, Ley R, Evans DJ, Almond JW, Barclay WS. The 5'-untranslated regions of
1206 picornavirus RNAs contain independent functional domains essential for RNA replication and
1207 translation. *J Virol* **68**, 4384-4391 (1994).
- 1208
1209 42. Rohll JB, Moon DH, Evans DJ, Almond JW. The 3' untranslated region of picornavirus RNA:
1210 features required for efficient genome replication. *J Virol* **69**, 7835-7844 (1995).
- 1211
1212 43. Bugaut A, Murat P, Balasubramanian S. An RNA hairpin to G-quadruplex conformational
1213 transition. *J Am Chem Soc* **134**, 19953-19956 (2012).
- 1214
1215 44. Harkness RWt, Mittermaier AK. G-quadruplex dynamics. *Biochim Biophys Acta Proteins*
1216 *Proteom* **1865**, 1544-1554 (2017).
- 1217
1218 45. Pagano A, *et al.* Common G-Quadruplex Binding Agents Found to Interact With i-Motif-
1219 Forming DNA: Unexpected Multi-Target-Directed Compounds. *Front Chem* **6**, (2018).
- 1220
1221 46. Rodriguez R, *et al.* Small-molecule-induced DNA damage identifies alternative DNA structures
1222 in human genes. *Nat Chem Biol* **8**, 301-310 (2012).
- 1223
1224 47. Zhang Y, *et al.* Native de novo structural determinations of non-canonical nucleic acid motifs
1225 by X-ray crystallography at long wavelengths. *Nucleic Acids Res* **48**, 9886-9898 (2020).
- 1226
1227 48. Banco MT, Ferre-D'Amare AR. The emerging structural complexity of G-quadruplex RNAs.
1228 *RNA* **27**, 390-402 (2021).
- 1229
1230 49. Kwok CK, Sahakyan AB, Balasubramanian S. Structural Analysis using SHALiPE to Reveal RNA
1231 G-Quadruplex Formation in Human Precursor MicroRNA. *Angew Chem Int Ed Engl* **55**, 8958-
1232 8961 (2016).
- 1233
1234 50. Hud NV, Smith FW, Anet FA, Feigon J. The selectivity for K⁺ versus Na⁺ in DNA quadruplexes
1235 is dominated by relative free energies of hydration: a thermodynamic analysis by 1H NMR.
1236 *Biochemistry-US* **35**, 15383-15390 (1996).
- 1237
1238 51. Guiset Miserachs H, Donghi D, Borner R, Johannsen S, Sigel RK. Distinct differences in metal
1239 ion specificity of RNA and DNA G-quadruplexes. *J Biol Inorg Chem* **21**, 975-986 (2016).
- 1240
1241 52. Saintome C, Amrane S, Mergny JL, Alberti P. The exception that confirms the rule: a higher-
1242 order telomeric G-quadruplex structure more stable in sodium than in potassium. *Nucleic*
1243 *Acids Res* **44**, 2926-2935 (2016).

- 1244
1245 53. Varizhuk AM, *et al.* Polymorphism of G4 associates: from stacks to wires via interlocks.
1246 *Nucleic Acids Res* **46**, 8978-8992 (2018).
- 1247
1248 54. Lim KW, Lacroix L, Yue DJ, Lim JK, Lim JM, Phan AT. Coexistence of two distinct G-quadruplex
1249 conformations in the hTERT promoter. *J Am Chem Soc* **132**, 12331-12342 (2010).
- 1250
1251 55. Fratta P, *et al.* C9orf72 hexanucleotide repeat associated with amyotrophic lateral sclerosis
1252 and frontotemporal dementia forms RNA G-quadruplexes. *Sci Rep* **2**, 1016 (2012).
- 1253
1254 56. Xu S, *et al.* Thioflavin T as an efficient fluorescence sensor for selective recognition of RNA G-
1255 quadruplexes. *Sci Rep* **6**, 24793 (2016).
- 1256
1257 57. Zhang J, Umemoto S, Nakatani K. Fluorescent indicator displacement assay for ligand-RNA
1258 interactions. *J Am Chem Soc* **132**, 3660-3661 (2010).
- 1259
1260 58. Del Villar-Guerra R, Gray RD, Trent JO, Chaires JB. A rapid fluorescent indicator displacement
1261 assay and principal component/cluster data analysis for determination of ligand-nucleic acid
1262 structural selectivity. *Nucleic Acids Res* **46**, e41 (2018).
- 1263
1264 59. Zhang S, *et al.* Real-time monitoring of DNA G-quadruplexes in living cells with a small-
1265 molecule fluorescent probe. *Nucleic Acids Res* **46**, 7522-7532 (2018).
- 1266
1267 60. Mohanty J, Barooah N, Dhamodharan V, Harikrishna S, Pradeepkumar PI, Bhasikuttan AC.
1268 Thioflavin T as an efficient inducer and selective fluorescent sensor for the human telomeric
1269 G-quadruplex DNA. *J Am Chem Soc* **135**, 367-376 (2013).
- 1270
1271 61. Koirala D, *et al.* A single-molecule platform for investigation of interactions between G-
1272 quadruplexes and small-molecule ligands. *Nat Chem* **3**, 782-787 (2011).
- 1273
1274 62. Kumar S, Choudhary D, Patra A, Bhavesh NS, Vivekanandan P. Analysis of G-quadruplexes
1275 upstream of herpesvirus miRNAs: evidence of G-quadruplex mediated regulation of KSHV
1276 miR-K12-1-9,11 cluster and HCMV miR-US33. *BMC Mol Cell Biol* **21**, 67 (2020).
- 1277
1278 63. Mestre-Fos S, *et al.* Profusion of G-quadruplexes on both subunits of metazoan ribosomes.
1279 *Plos One* **14**, e0226177 (2019).
- 1280
1281 64. Harutyunyan S, *et al.* Viral uncoating is directional: exit of the genomic RNA in a common
1282 cold virus starts with the poly-(A) tail at the 3'-end. *Plos Pathog* **9**, e1003270 (2013).
- 1283
1284 65. Harutyunyan S, Kowalski H, Blaas D. The Rhinovirus subviral a-particle exposes 3'-terminal
1285 sequences of its genomic RNA. *J Virol* **88**, 6307-6317 (2014).
- 1286

- 1287 66. Brandenburg B, Lee LY, Lakadamyali M, Rust MJ, Zhuang X, Hogle JM. Imaging poliovirus
1288 entry in live cells. *PLoS Biol* **5**, e183 (2007).
- 1289
1290 67. Rowlands DJ, Sangar DV, Brown F. Buoyant density of picornaviruses in caesium salts. *J Gen*
1291 *Viol* **13**, 141-152 (1971).
- 1292
1293 68. Reisdorph N, *et al.* Human rhinovirus capsid dynamics is controlled by canyon flexibility.
1294 *Virology* **314**, 34-44 (2003).
- 1295
1296 69. Kremser L, Okun VM, Nicodemou A, Blaas D, Kenndler E. Binding of fluorescent dye to
1297 genomic RNA inside intact human rhinovirus after viral capsid penetration investigated by
1298 capillary electrophoresis. *Anal Chem* **76**, 882-887 (2004).
- 1299
1300 70. Katpally U, Smith TJ. Pocket factors are unlikely to play a major role in the life cycle of human
1301 rhinovirus. *J Virol* **81**, 6307-6315 (2007).
- 1302
1303 71. Real-Hohn A, *et al.* Catching Common Cold Virus with a Net: Pyridostatin Forms Filaments in
1304 Tris Buffer That Trap Viruses-A Novel Antiviral Strategy? *Viruses* **12**, (2020).
- 1305
1306 72. Walter TS, Ren J, Tuthill TJ, Rowlands DJ, Stuart DI, Fry EE. A plate-based high-throughput
1307 assay for virus stability and vaccine formulation. *J Virol Methods* **185**, 166-170 (2012).
- 1308
1309 73. Real-Hohn A, Groznica M, Loffler N, Blaas D, Kowalski H. nanoDSF: In vitro Label-Free Method
1310 to Monitor Picornavirus Uncoating and Test Compounds Affecting Particle Stability. *Front*
1311 *Microbiol* **11**, 1442 (2020).
- 1312
1313 74. Rowlands DJ, Sangar DV, Brown F. A comparative chemical and serological study of the full
1314 and empty particles of foot-and mouth disease virus. *J Gen Virol* **26**, 227-238 (1975).
- 1315
1316 75. Frisby DP, Cotter RI, Richards BM. Structural studies of encephalomyocarditis virus RNA both
1317 in situ and in free solution. *J Gen Virol* **37**, 311-322 (1977).
- 1318
1319 76. Hewat EA, Blaas D. Nonneutralizing human rhinovirus serotype 2-specific monoclonal
1320 antibody 2G2 attaches to the region that undergoes the most dramatic changes upon release
1321 of the viral RNA. *J Virol* **80**, 12398-12401 (2006).
- 1322
1323 77. Kremser L, Petsch M, Blaas D, Kenndler E. Capillary electrophoresis of affinity complexes
1324 between subviral 80S particles of human rhinovirus and monoclonal antibody 2G2.
1325 *Electrophoresis* **27**, 2630-2637 (2006).
- 1326
1327 78. Lonberg-Holm K, Noble-Harvey J. Comparison of in vitro and cell-mediated alteration of a
1328 human Rhinovirus and its inhibition by sodium dodecyl sulfate. *J Virol* **12**, 819-826 (1973).
- 1329

- 1330 79. Zhang LJ, Fedorov Y, Adams D, Lin F. Identification of complement inhibitory activities of two
1331 chemotherapeutic agents using a high-throughput cell imaging-based screening assay. *Mol*
1332 *Immunol* **101**, 86-91 (2018).
- 1333
1334 80. Piazza A, *et al.* Genetic instability triggered by G-quadruplex interacting Phen-DC compounds
1335 in *Saccharomyces cerevisiae*. *Nucleic Acids Res* **38**, 4337-4348 (2010).
- 1336
1337 81. Endoh T, Sugimoto N. Conformational Dynamics of the RNA G-Quadruplex and its Effect on
1338 Translation Efficiency. *Molecules* **24**, (2019).
- 1339
1340 82. Warner J, Madden MJ, Darnell JE. The interaction of poliovirus RNA with *Escherichia coli*
1341 ribosomes. *Virology* **19**, 393-399 (1963).
- 1342
1343 83. Fout GS, Medappa KC, Mapoles JE, Rueckert RR. Radiochemical determination of polyamines
1344 in poliovirus and human rhinovirus 14. *J Biol Chem* **259**, 3639-3643 (1984).
- 1345
1346 84. Koch F, Koch G. *The molecular biology of poliovirus*. Springer (1985).
- 1347
1348 85. Li P, *et al.* Integrative Analysis of Zika Virus Genome RNA Structure Reveals Critical
1349 Determinants of Viral Infectivity. *Cell Host Microbe* **24**, 875-886 e875 (2018).
- 1350
1351 86. Ziv O, *et al.* The Short- and Long-Range RNA-RNA Interactome of SARS-CoV-2. *Mol Cell* **80**,
1352 1067-1077 e1065 (2020).
- 1353
1354 87. Walter F, Putz J, Giege R, Westhof E. Binding of tobramycin leads to conformational changes
1355 in yeast tRNA(Asp) and inhibition of aminoacylation. *EMBO J* **21**, 760-768 (2002).
- 1356
1357 88. Serganov A, Patel DJ. Molecular recognition and function of riboswitches. *Curr Opin Struct*
1358 *Biol* **22**, 279-286 (2012).
- 1359
1360 89. Rozov A, *et al.* Importance of potassium ions for ribosome structure and function revealed by
1361 long-wavelength X-ray diffraction. *Nat Commun* **10**, 2519 (2019).
- 1362
1363 90. Silvers R, Keller H, Schwalbe H, Hengesbach M. Differential scanning fluorimetry for
1364 monitoring RNA stability. *Chembiochem* **16**, 1109-1114 (2015).
- 1365
1366 91. Kwok CK, Marsico G, Sahakyan AB, Chambers VS, Balasubramanian S. rG4-seq reveals
1367 widespread formation of G-quadruplex structures in the human transcriptome. *Nat Methods*
1368 **13**, 841-844 (2016).
- 1369
1370 92. Ojosnegros S, *et al.* Viral genome segmentation can result from a trade-off between genetic
1371 content and particle stability. *PLoS Genet* **7**, e1001344 (2011).

1372
1373 93. Speir JA, Johnson JE. Nucleic acid packaging in viruses. *Curr Opin Struct Biol* **22**, 65-71 (2012).

1374
1375 94. Brabec-Zaruba M, Pfanzagl B, Blaas D, Fuchs R. Site of human rhinovirus RNA uncoating
1376 revealed by fluorescent in situ hybridization. *J Virol* **83**, 3770-3777 (2009).

1377
1378 95. Krenn BM, Holzer B, Gaudernak E, Triendl A, van Kuppeveld FJ, Seipelt J. Inhibition of
1379 polyprotein processing and RNA replication of human rhinovirus by pyrrolidine
1380 dithiocarbamate involves metal ions. *J Virol* **79**, 13892-13899 (2005).

1381
1382 96. Real-Hohn A, *et al.* Impairing the function of MLCK, myosin Va or myosin Vb disrupts
1383 Rhinovirus B14 replication. *Sci Rep* **7**, 17153 (2017).

1384
1385 97. Fuchs R, Blaas D. Uncoating of human rhinoviruses. *Rev Med Virol* **20**, 281-297 (2010).

1386
1387 98. Malgowska M, Czajczynska K, Gudanis D, Tworak A, Gdaniec Z. Overview of the RNA G-
1388 quadruplex structures. *Acta Biochim Pol* **63**, 609-621 (2016).

1389
1390 99. Weiss VU, *et al.* Capillary electrophoresis, gas-phase electrophoretic mobility molecular
1391 analysis, and electron microscopy: effective tools for quality assessment and basic rhinovirus
1392 research. *Methods Mol Biol* **1221**, 101-128 (2015).

1393
1394 100. Rodriguez R, *et al.* Small-molecule-induced DNA damage identifies alternative DNA structures
1395 in human genes. *Nat Chem Biol* **8**, 301-310 (2012).

1396
1397 101. Bao HL, Xu Y. Investigation of higher-order RNA G-quadruplex structures in vitro and in living
1398 cells by ¹⁹F NMR spectroscopy. *Nat Protoc* **13**, 652-665 (2018).

1399
1400 102. Husby J, Todd AK, Platts JA, Neidle S. Small-Molecule G-Quadruplex Interactions: Systematic
1401 Exploration of Conformational Space Using Multiple Molecular Dynamics. *Biopolymers* **99**,
1402 989-1005 (2013).

1403
1404 103. Rocca R, *et al.* Molecular recognition of a carboxy pyridostatin toward G-quadruplex
1405 structures: Why does it prefer RNA? *Chem Biol Drug Des* **90**, 919-925 (2017).

1406
1407 104. Carvalho J, *et al.* Ligand screening to pre-miRNA 149 G-quadruplex investigated by molecular
1408 dynamics. *J Biomol Struct Dyn* **38**, 2276-2286 (2020).

1409
1410 105. Bradley DF, Wolf MK. Aggregation of Dyes Bound to Polyanions. *Proc Natl Acad Sci U S A* **45**,
1411 944-952 (1959).

1412

- 1413 106. Gai W, *et al.* A dual-site simultaneous binding mode in the interaction between parallel-
1414 stranded G-quadruplex [d(TGGGGT)]₄ and cyanine dye 2,2'-diethyl-9-methyl-
1415 selenacarboyanine bromide. *Nucleic Acids Res* **41**, 2709-2722 (2012).
- 1416
1417 107. Deiana M, Jamroskovic J, Obi I, Sabouri N. Unravelling the cellular emission fingerprint of the
1418 benchmark G-quadruplex-interactive compound Phen-DC3. *Chem Commun (Camb)* **56**,
1419 14251-14254 (2020).
- 1420
1421 108. Broo K, *et al.* Viral capsid mobility: a dynamic conduit for inactivation. *Proc Natl Acad Sci U S*
1422 *A* **98**, 2274-2277 (2001).
- 1423
1424 109. Chandler-Bostock R, *et al.* Assembly of infectious enteroviruses depends on multiple,
1425 conserved genomic RNA-coat protein contacts. *Plos Pathog* **16**, e1009146 (2020).
- 1426
1427 110. Cheng CH, Ishii K, Tahara T. Microsecond Equilibrium Dynamics of Hairpin-Forming
1428 Oligonucleotides Quantified by Two-Color Two-Dimensional Fluorescence Lifetime
1429 Correlation Spectroscopy. *J Phys Chem B* **124**, 10673-10681 (2020).
- 1430
1431 111. Zhang AY, Balasubramanian S. The kinetics and folding pathways of intramolecular G-
1432 quadruplex nucleic acids. *J Am Chem Soc* **134**, 19297-19308 (2012).
- 1433
1434 112. Nugent CI, Johnson KL, Sarnow P, Kirkegaard K. Functional coupling between replication and
1435 packaging of poliovirus replicon RNA. *J Virol* **73**, 427-435 (1999).
- 1436
1437 113. Conn GL, Gittis AG, Lattman EE, Misra VK, Draper DE. A compact RNA tertiary structure
1438 contains a buried backbone-K⁺ complex. *J Mol Biol* **318**, 963-973 (2002).
- 1439
1440 114. Basu S, *et al.* A specific monovalent metal ion integral to the AA platform of the RNA
1441 tetraloop receptor. *Nature Structural Biology* **5**, 986-992 (1998).
- 1442
1443 115. Ghribi S, Maurel MC, Rougee M, Favre A. Evidence for tertiary structure in natural single
1444 stranded RNAs in solution. *Nucleic Acids Res* **16**, 1095-1112 (1988).
- 1445
1446 116. Wang SR, *et al.* A highly conserved G-rich consensus sequence in hepatitis C virus core gene
1447 represents a new anti-hepatitis C target. *Sci Adv* **2**, e1501535 (2016).
- 1448
1449 117. Huang Y, Hogle JM, Chow M. Is the 135S poliovirus particle an intermediate during cell entry?
1450 *J Virol* **74**, 8757-8761 (2000).
- 1451
1452 118. Karunatilaka KS, Filman DJ, Strauss M, Loparo JJ, Hogle JM. Real-Time Imaging of Polioviral
1453 RNA Translocation across a Membrane. *mBio* **12**, (2021).
- 1454

- 1455 119. Zhang X, *et al.* Mimicking Ribosomal Unfolding of RNA Pseudoknot in a Protein Channel. *J Am*
1456 *Chem Soc* **137**, 15742-15752 (2015).
- 1457
1458 120. Endoh T, Kawasaki Y, Sugimoto N. Suppression of Gene Expression by G-Quadruplexes in
1459 Open Reading Frames Depends on G-Quadruplex Stability. *Angewandte Chemie International*
1460 *Edition* **52**, 5522-5526 (2013).
- 1461
1462 121. Ren J, *et al.* Picornavirus uncoating intermediate captured in atomic detail. *Nat Commun* **4**,
1463 1929 (2013).
- 1464
1465 122. Polson JM, McLure ZRN. Free-energy cost of localizing a single monomer of a confined
1466 polymer. *Physical Review E* **99**, 062503 (2019).
- 1467
1468 123. Indelicato G, Cermelli P, Twarock R. A coarse-grained model of the expansion of the human
1469 rhinovirus 2 capsid reveals insights in genome release. *J R Soc Interface* **16**, 20190044 (2019).
- 1470
1471 124. Dai X, *et al.* In situ structures of the genome and genome-delivery apparatus in a single-
1472 stranded RNA virus. *Nature* **541**, 112-116 (2017).
- 1473
1474 125. Wilson JN, Cooper PD. Aspects of the growth of poliovirus as revealed by the photodynamic
1475 effects of neutral red and acridine orange. *Virology* **21**, 135-145 (1963).
- 1476
1477 126. Schaffer FL. Binding of proflavine by and photoinactivation of poliovirus propagated in the
1478 presence of the dye. *Virology* **18**, 412-425 (1962).
- 1479
1480 127. Danthi P, Tosteson M, Li QH, Chow M. Genome delivery and ion channel properties are
1481 altered in VP4 mutants of poliovirus. *J Virol* **77**, 5266-5274 (2003).
- 1482
1483 128. Hrebík D, *et al.* ICAM-1 induced rearrangements of capsid and genome prime rhinovirus 14
1484 for activation and uncoating. *Proceedings of the National Academy of Sciences* **118**,
1485 e2024251118 (2021).
- 1486
1487 129. Zhang M, *et al.* Optimized photochemistry enables efficient analysis of dynamic RNA
1488 structuromes and interactomes in genetic and infectious diseases. *Nat Commun* **12**, 2344
1489 (2021).
- 1490
1491 130. Chen X-C, *et al.* Tracking the Dynamic Folding and Unfolding of RNA G-Quadruplexes in Live
1492 Cells. *Angewandte Chemie International Edition* **57**, 4702-4706 (2018).
- 1493
1494 131. Chen MC, Murat P, Abecassis K, Ferré-D'Amaré AR, Balasubramanian S. Insights into the
1495 mechanism of a G-quadruplex-unwinding DEAH-box helicase. *Nucleic Acids Res* **43**, 2223-
1496 2231 (2015).
- 1497

- 1498 132. Mendoza O, Bourdoncle A, Boule JB, Brosh RM, Jr., Mergny JL. G-quadruplexes and helicases.
1499 *Nucleic Acids Res* **44**, 1989-2006 (2016).
- 1500
1501 133. Xia H, *et al.* Human Enterovirus Nonstructural Protein 2CATPase Functions as Both an RNA
1502 Helicase and ATP-Independent RNA Chaperone. *Plos Pathog* **11**, e1005067 (2015).
- 1503
1504 134. Piazza A, *et al.* Non-Canonical G-quadruplexes cause the hCEB1 minisatellite instability in
1505 *Saccharomyces cerevisiae*. *Elife* **6**, (2017).
- 1506
1507 135. Hirashima K, Seimiya H. Telomeric repeat-containing RNA/G-quadruplex-forming sequences
1508 cause genome-wide alteration of gene expression in human cancer cells in vivo. *Nucleic Acids*
1509 *Res* **43**, 2022-2032 (2015).
- 1510
1511 136. Blake K, O'Connell S. *Virus culture*. Blackwell Scientific Publications (1993).
- 1512
1513 137. Skern T, *et al.* A neutralizing epitope on human rhinovirus type 2 includes amino acid
1514 residues between 153 and 164 of virus capsid protein VP2. *J Gen Virol* **68 (Pt 2)**, 315-323
1515 (1987).
- 1516
1517 138. Corbic Ramljak I, *et al.* Cellular N-myristoyltransferases play a crucial picornavirus genus-
1518 specific role in viral assembly, virion maturation, and infectivity. *Plos Pathog* **14**, e1007203
1519 (2018).
- 1520
1521 139. Piotto M, Saudek V, Sklenar V. Gradient-tailored excitation for single-quantum NMR
1522 spectroscopy of aqueous solutions. *J Biomol NMR* **2**, 661-665 (1992).

1523

1524

1525 FIGURES LEGENDS

1526 **Figure 1. The genomic RNA of all RVs harbours sequences with the propensity to form**
1527 **GQs. This is confirmed for those two with the highest and lowest G-score from RV-A2**
1528 **via nuclear magnetic resonance and circular dichroism.** (a) RNA sequences of 120 RVs
1529 available in the NCBI database were analysed for putative GQ forming sequences by using a
1530 local copy of the QGRS mapper. G-scores ≥ 10 are shown as rectangles with their length
1531 corresponding to the length of the putative GQ. The colour corresponds to the respective G-
1532 score as indicated with the colour key bar. Note that the sequences were used without
1533 alignment optimisation, i.e. neither deletions nor insertions were taken into account. Asterisks
1534 denote highly conserved GQs. Species RV-A, RV-B, and RV-C are specified. (b) One-
1535 dimensional $^1\text{H-NMR}$ spectra of ribonucleotides representing putative two-layered GQ-
1536 forming sequences of RV-A2 with the lowest G-score (G11) and the highest G-score (G20),

1537 both at 0.25 mM in 10 mM sodium phosphate (pH 7.4), 100 mM KCl. In addition, the
1538 chemical shift region characteristic of imino protons involved in Hoogsteen base pairing
1539 (salmon coloured box) and the Watson-Crick base pair region (olive coloured box) are
1540 indicated. NMR spectra were measured at different temperatures (277 K and 307 K) and
1541 after adding PDS to 0.5 mM (i.e. a stoichiometry of 1:2) final concentration. (c) CD
1542 spectroscopy of miniTERRA, G11, and G20 diluted in 100 mM sodium phosphate buffer (pH
1543 7.4) or 100 mM potassium phosphate buffer (pH 7.4) to 20 μ M reveals an all-parallel RNA
1544 strand orientation, irrespective of the cation present in the buffer.

1545

1546 **Figure 2. Biophysical characterisation of miniTERRA (control GQ), RV-A2 GQ G11 and**
1547 **G20 and impact of K⁺, Na⁺ and PDS.** Ribooligonucleotides dissolved at 5 μ M either in 100
1548 mM sodium phosphate buffer (pH 7.4) (a - left panels) and (b) or in 100 mM potassium
1549 phosphate buffer (pH 7.4) (a - right panels) and (c). (a) CD melting profiles of G11, G20, and
1550 miniTERRA measured at 265 nm; the trace for unfolding is red and refolding in blue. The
1551 temperature was ramped up or decreased at a rate of 1 $^{\circ}$ C per min and the corresponding
1552 unfolded state fraction is shown in the left subpanels for each cation (Na⁺, K⁺) as normalised
1553 ellipticity (θ). The second-order derivative of the respective curves is presented in the right
1554 subpanels. (b) Left panel: The same ribooligonucleotides dissolved in 100 mM sodium
1555 phosphate buffer (pH 7.4) were incubated with ThT, and the fluorescence was measured at
1556 490 nm (n = 3). Right panel: Ribooligonucleotides identically pre-incubated with ThT were
1557 titrated with PDS, the fluorescence was measured after each addition and normalised to the
1558 initial fluorescence signal (i.e. without PDS = 100 %; n = 3). (c) The same experiment as in
1559 (b) with ribooligonucleotides dissolved in 100 mM potassium phosphate buffer (pH 7.4).

1560

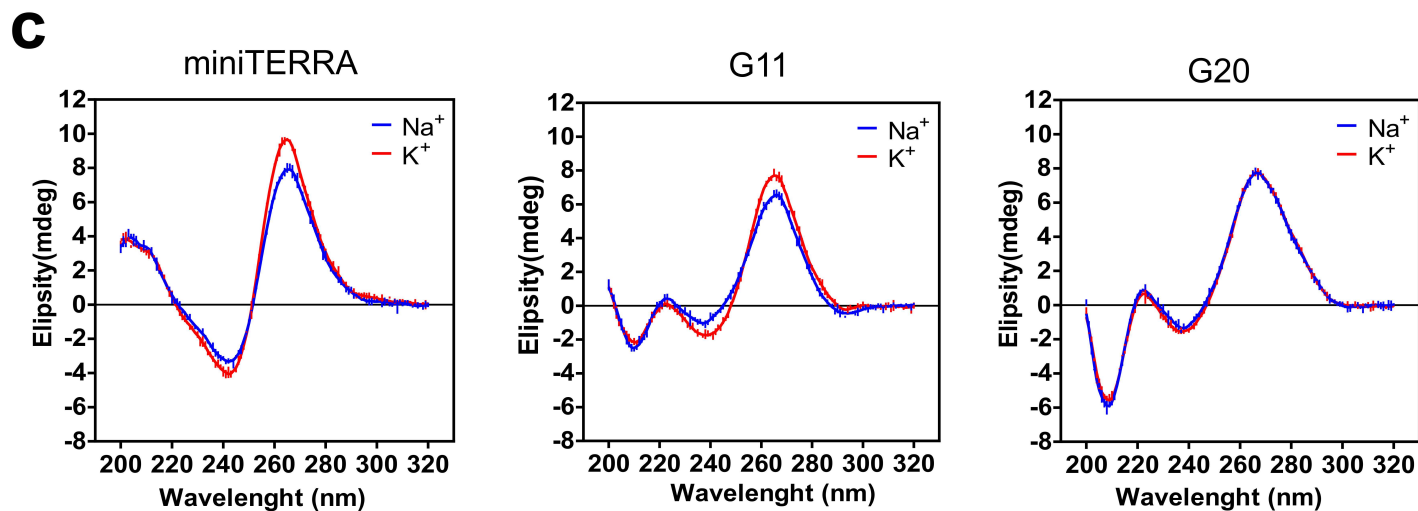
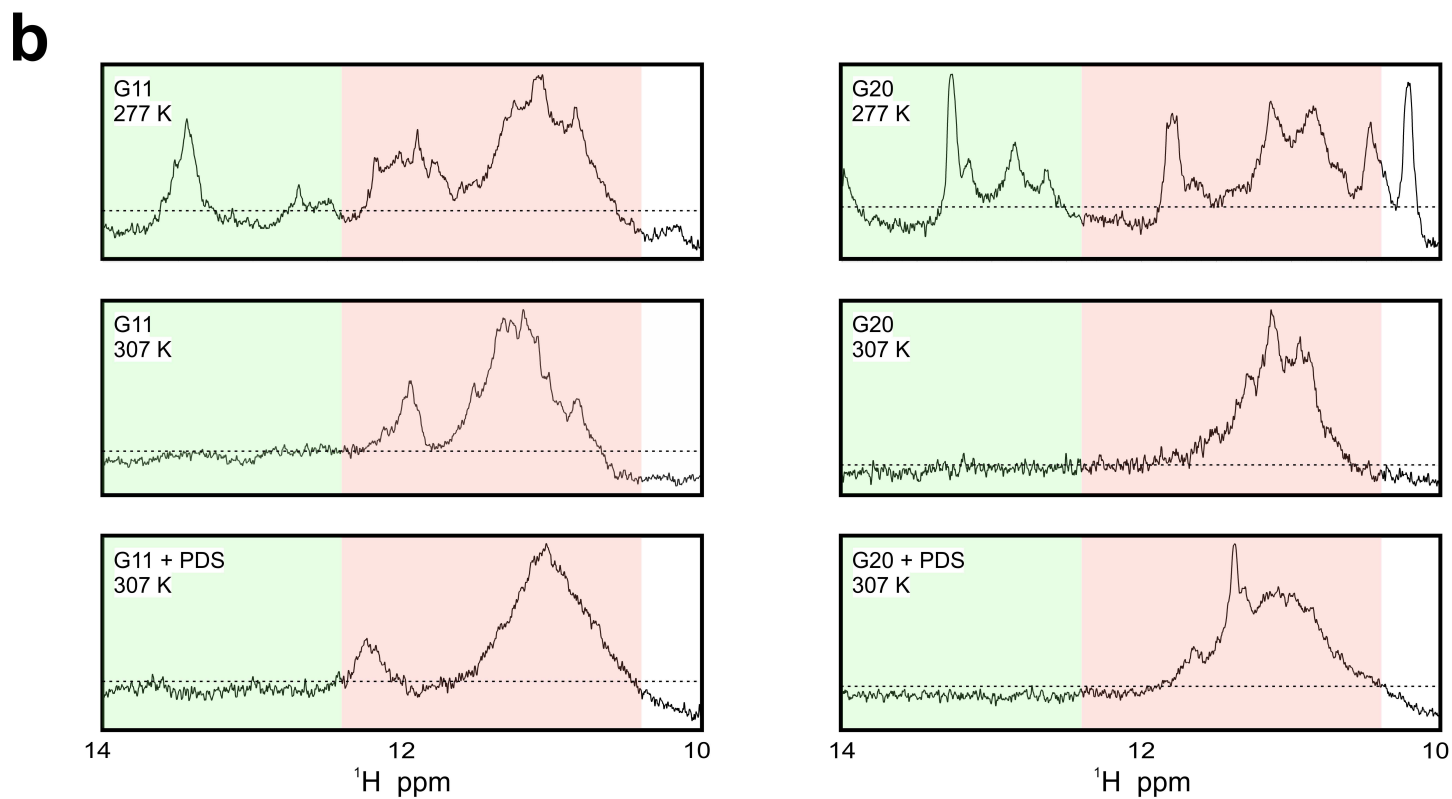
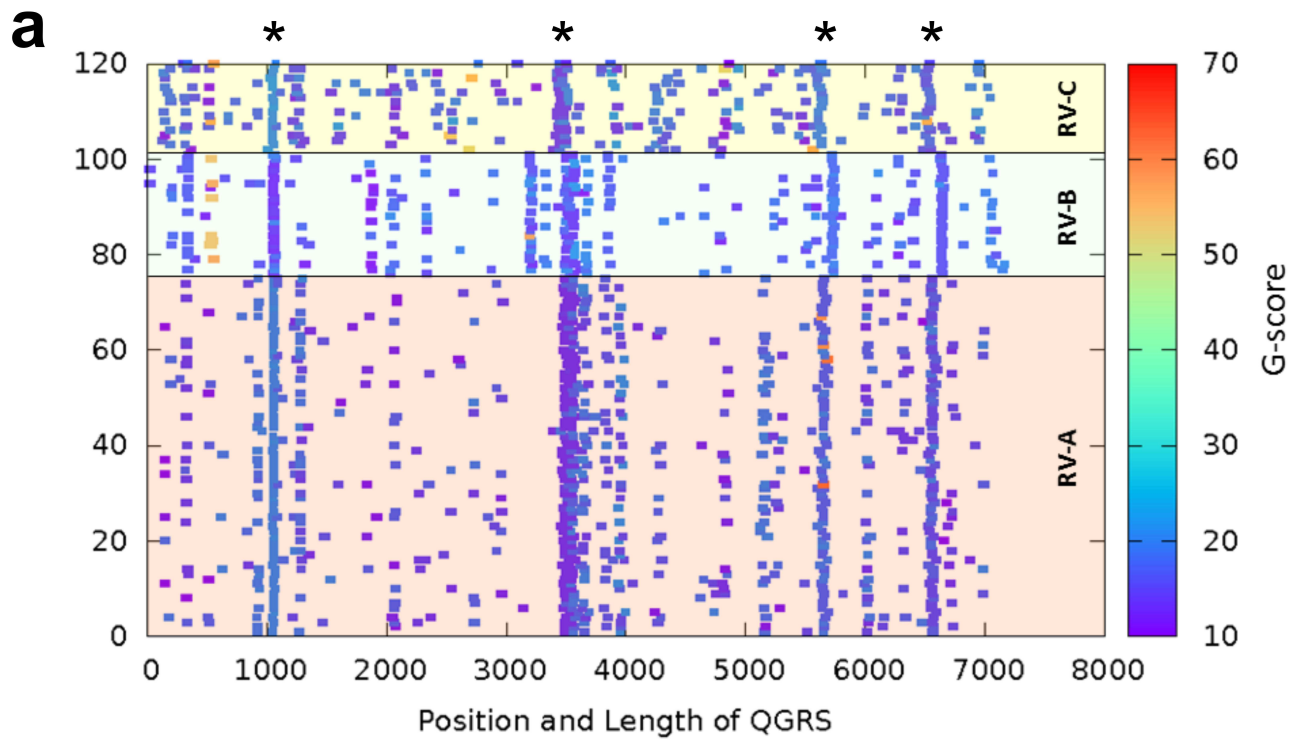
1561 **Figure 3. GQ-binding compounds increase RV-A2 capsid permeability, impair**
1562 **uncoating, and decrease infectivity.** (a) Scatter plot of the temperature of onset (T_{on}) of
1563 capsid permeability for SYTO 82 determined in a PaSTRy with purified RV-A2 that had been
1564 pre-incubated \pm 200 μ M PDS at 34 $^{\circ}$ C for 4 h (for the raw data, see Supplementary Fig. S1; n
1565 = 6). (b and c) HeLa cells were infected with purified RV-A2 that had been pre-incubated \pm
1566 200 μ M PDS at 34 $^{\circ}$ C for 4 h. Thirty min pi, cells were harvested, and the intracellular virus
1567 was released by three cycles of freezing and thawing and separated from cellular debris by
1568 low-speed centrifugation. The cleared native and subviral particle-containing supernatant
1569 was subjected to immunoprecipitation with mAb 2G2 specific for A- and B-particles (b and c).
1570 (b) Proteins in the samples were separated by SDS-PAGE (10 %) followed by Western
1571 blotting using anti-VP2 mAb 8F5 and a goat anti-mouse IgG HRP-conjugated secondary
1572 antibody, and bands were quantified by densitometry. (c) RNA in the samples was isolated,
1573 reverse transcribed and subjected to qPCR using specific primers. The quantity of RV-A2

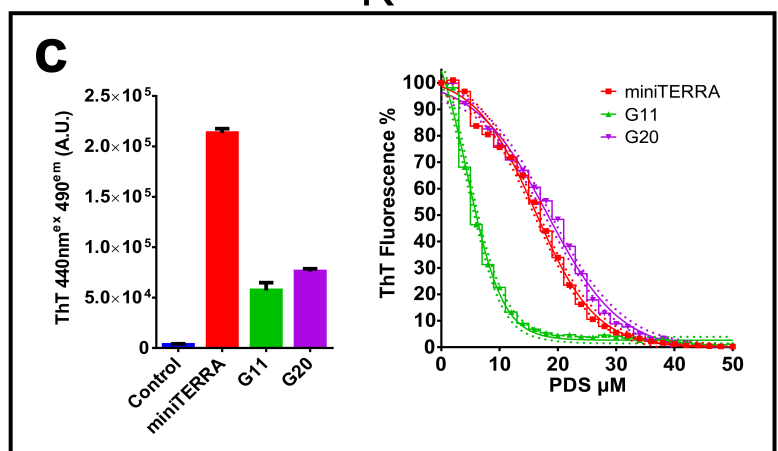
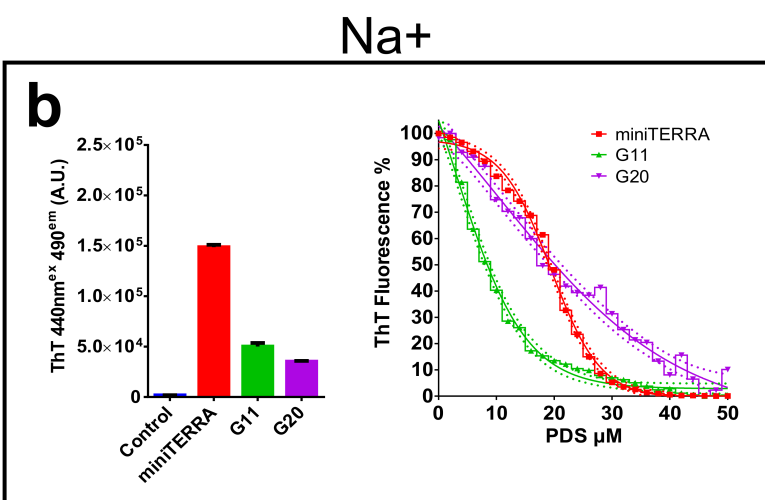
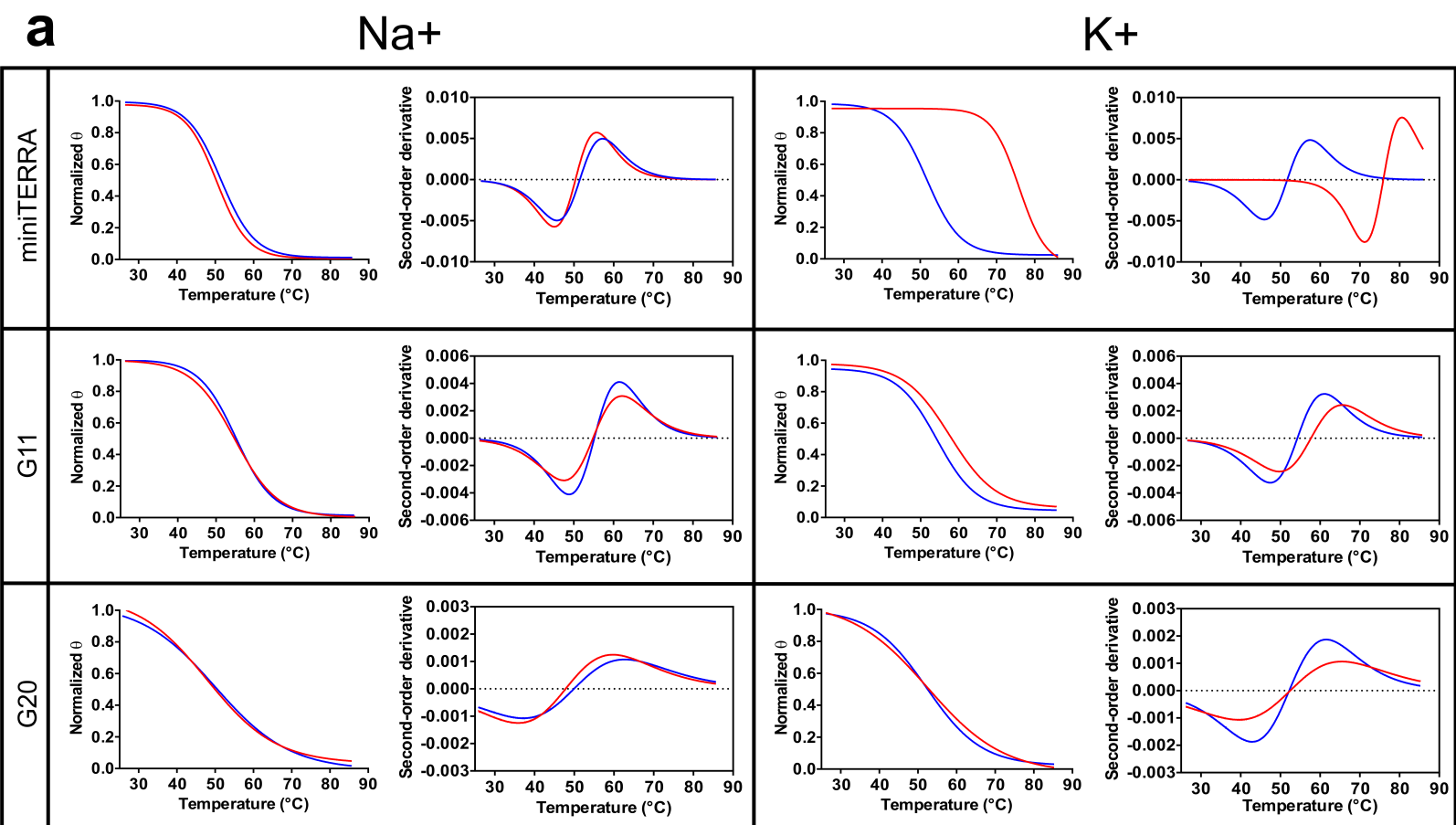
1574 RNA was normalised by relating the Ct value to the one obtained for a known amount of AiV
1575 seed virus that had been added to all cleared supernatant samples prior to the RNA isolation.
1576 (d) Cleared supernatants prepared as above were separated by 10 – 40 % (w/v) sucrose
1577 density gradient centrifugation. Fifteen fractions were collected from top to bottom, proteins
1578 were heat-denatured, dot blots were prepared, and viral material was quantified with mAb
1579 8F5 and IRDye 680RD goat anti-mouse IgG secondary antibody (n = 3). The obtained signal
1580 intensity was plotted against the gradient fraction (250 µl each of a total of 5 ml) from top to
1581 bottom. Note that VP2 is present in all (sub)viral particles. Native virus (150S) and subviral B-
1582 particles (80S) generated *in vitro* by heating of RV-A2 to 56 °C for 10 min were used as
1583 sedimentation controls and run on separate gradients. Their position is indicated in the plot;
1584 the position of the 14S pentamers was inferred from the literature. (e) Purified RV-A2 was
1585 incubated ± PDS or Phen-DC3 at the concentrations indicated for 4 h at 34 °C. The
1586 compounds, which have not entered the virion were removed from the samples by centrifugal
1587 ultrafiltration followed by multiple washing steps to eliminate any external traces of the
1588 compound; the (un)treated virus material was then used to infect HeLa cells. The percentage
1589 of infected cells was determined at 9 h pi by FACS analysis of the intracellularly produced
1590 VP2 with the mAb 8F5 and a secondary anti-mouse AlexaFluor 488 conjugated secondary
1591 antibody and is indicated as bars (n = 3; * p ≤ 0.05; ** p ≤ 0.01; NS, not significant).

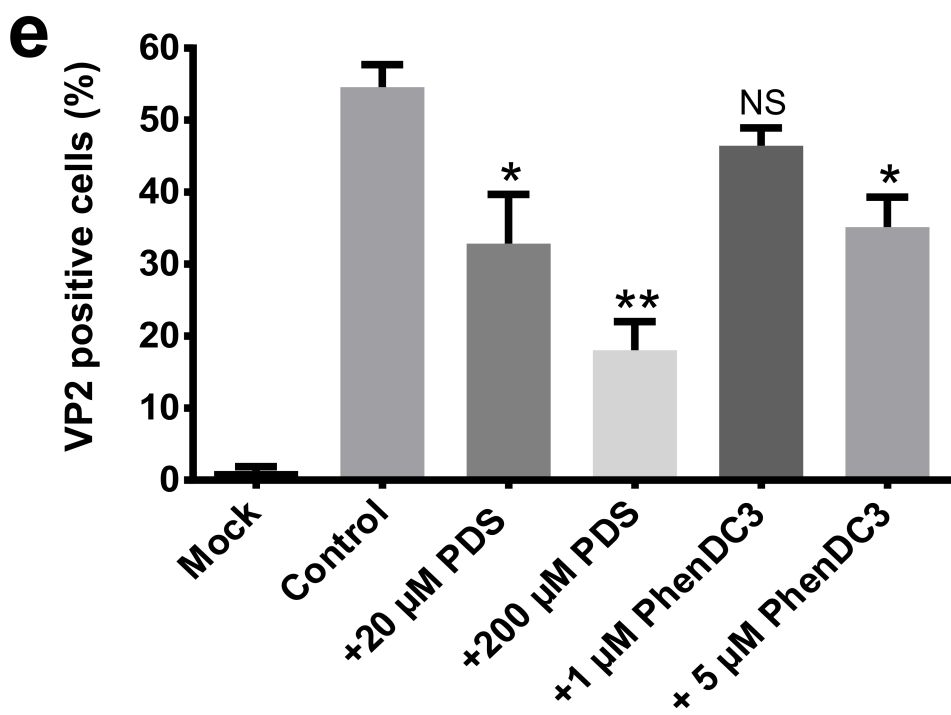
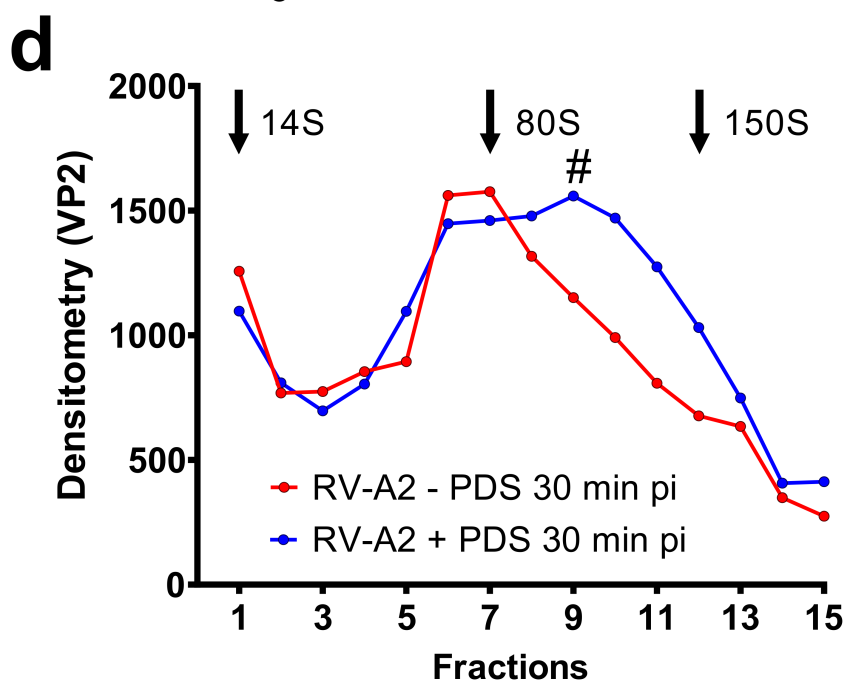
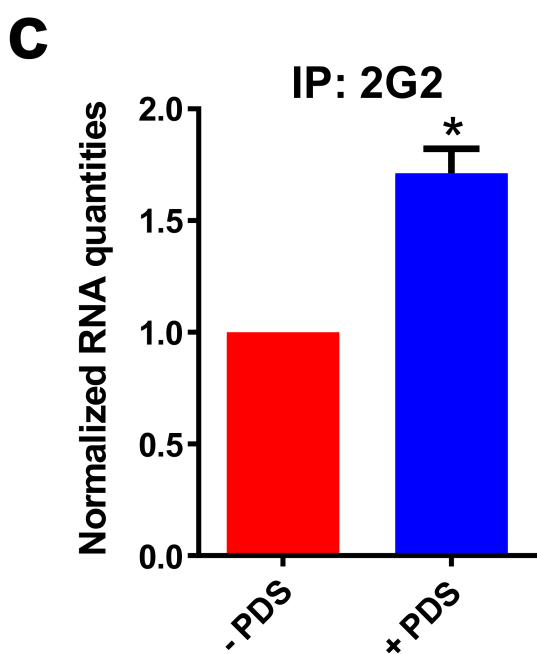
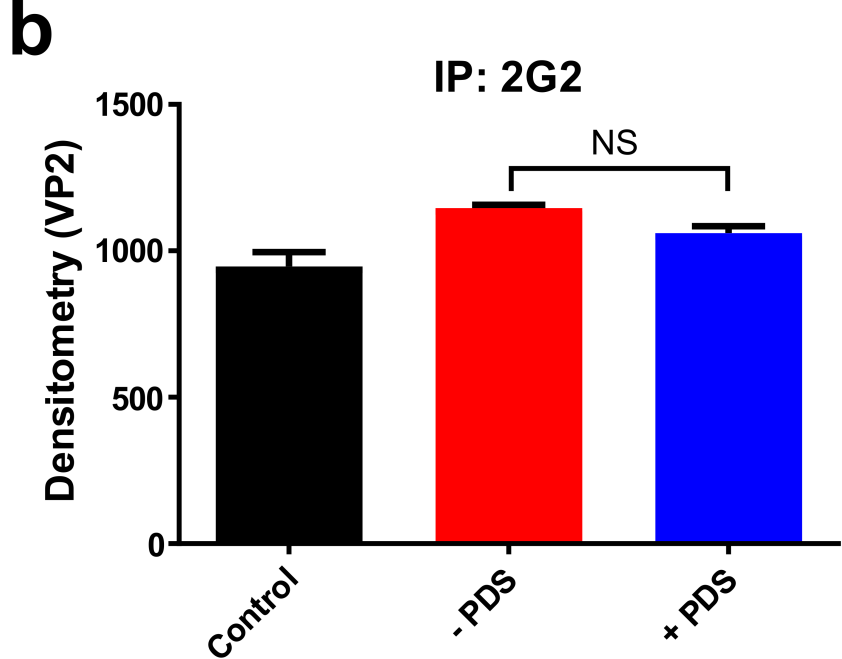
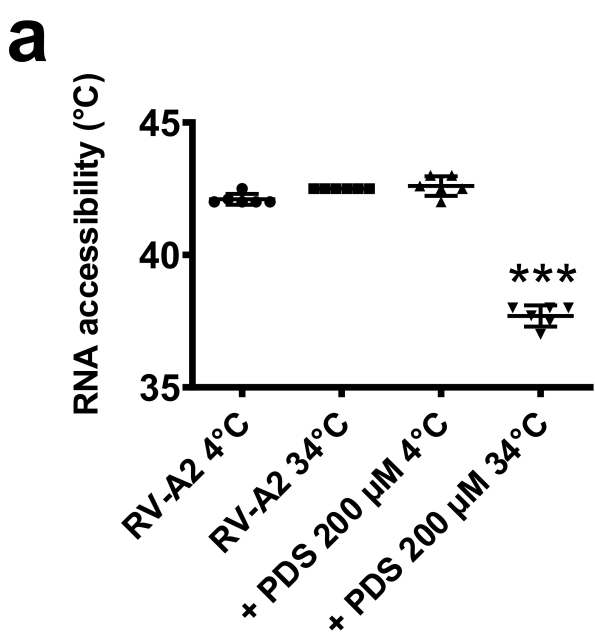
1592

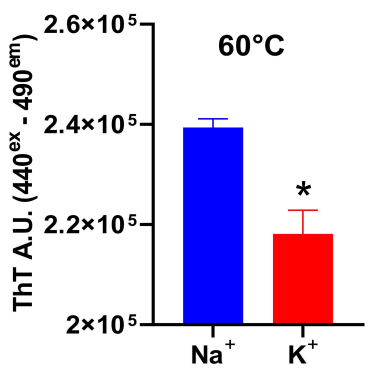
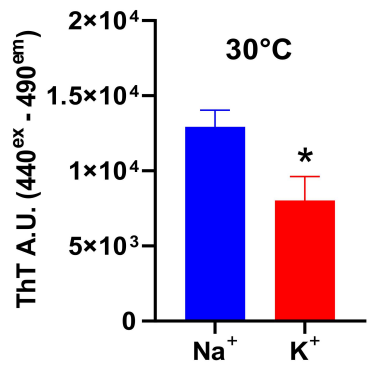
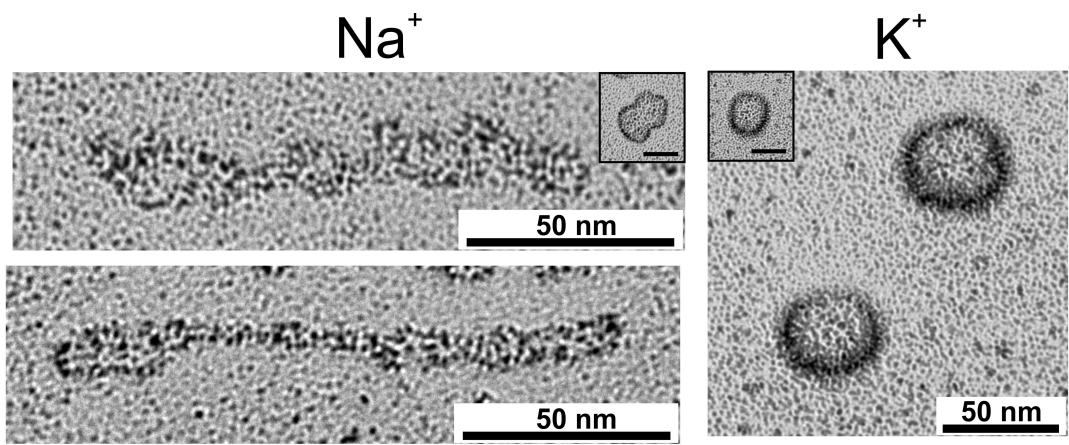
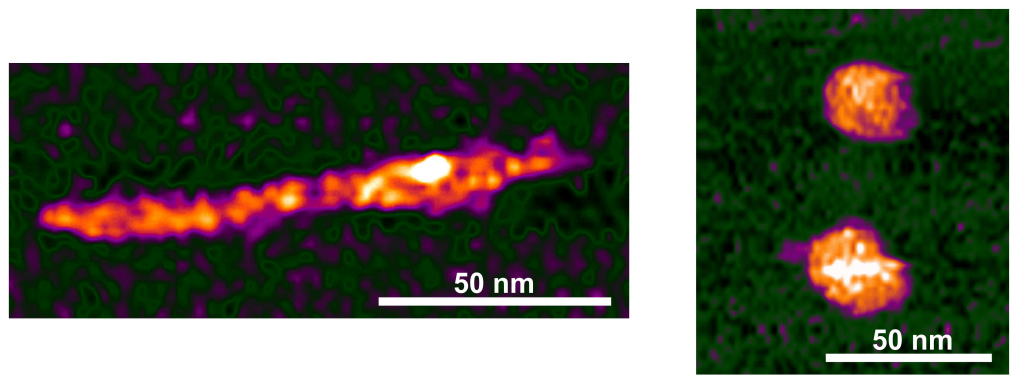
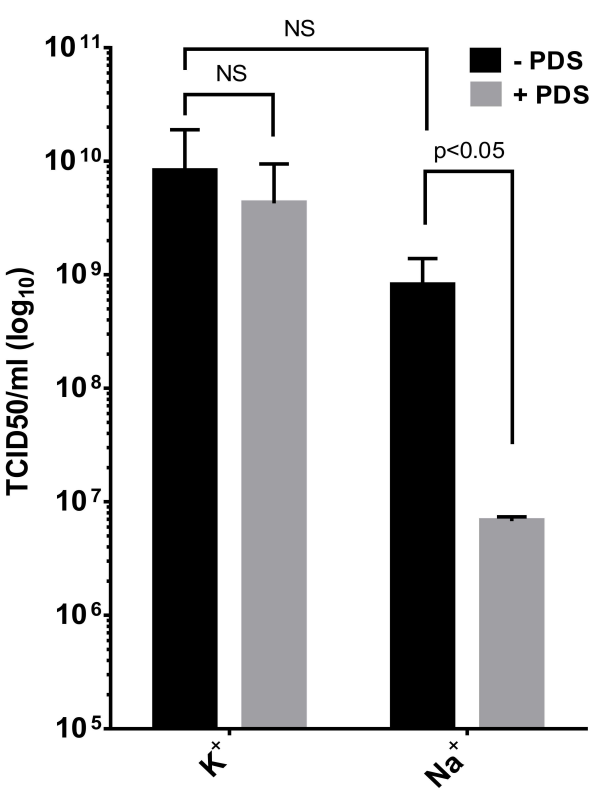
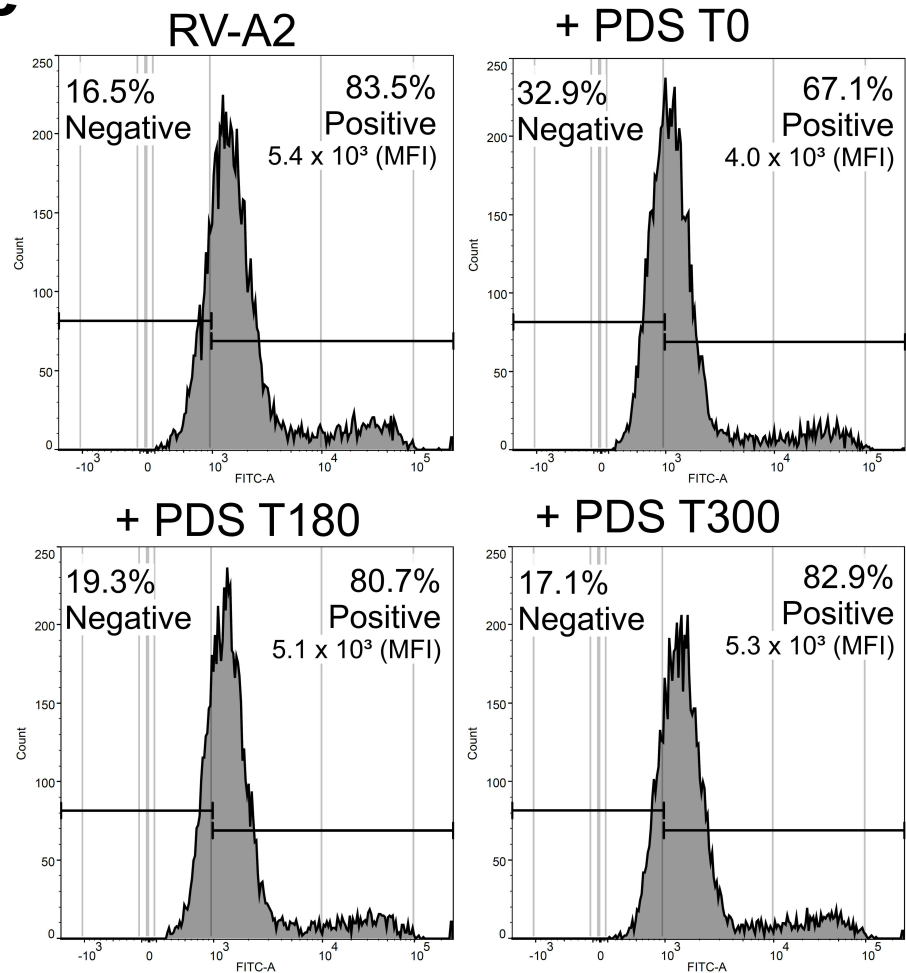
1593 **Figure 4. PDS treatment of ex virion RNA results in a drastic PDS-induced re-**
1594 **organisation in the presence of sodium but not potassium ions.** (a) RV-A2 RNA was
1595 gently released into solution by proteolysis of the capsid protein shell in 100 mM sodium
1596 phosphate buffer (Na⁺) or 100 mM potassium phosphate buffer (K⁺). The ex virion RNA
1597 samples were mixed with ThT (final concentration 5 µM), and the ThT fluorescence signal
1598 acquired at 30 °C. Afterwards, samples were incubated for 10 min at 60 °C and cooled to
1599 room temperature on the bench for 30 min, followed by ThT fluorescence acquisition. (b) RV-
1600 A2 RNA (prepared identically as in (a)) was incubated with 20 µM PDS for 10 min at room
1601 temperature and subjected to rotary shadowing followed by TEM. Inserts depicting
1602 representative images of ex virion RNA in sodium or potassium phosphate buffers non-
1603 treated with PDS are displayed (50 nm scale bar). (c) Samples similarly treated as in (b)
1604 were analysed by AFM in the presence of 100 mM sodium or potassium phosphate buffer.
1605 (d) Purified RV-A2 was diluted in the same buffers as above and incubated overnight with or
1606 without 20 µM PDS at room temperature. Unbound PDS was removed by centrifugal
1607 ultrafiltration and the infectivity of the samples was determined by end-point titration. The
1608 viral titer measured as TCID₅₀ is rendered by a bar graph (n = 3). The significance of the
1609 differences was evaluated by two-way ANOVA; NS – statistically not significant (p ≥ 0.05). (e)
1610 HeLa cells were seeded in six-well plates and cultivated at 37 °C until 70 - 80 % confluent on

1611 the day of the experiment. Cells were then challenged with RV-A2 (MOI = 10) for 30 min at 4
1612 °C, allowing virus attachment. Synchronised virus entry was triggered by transfer into a 34
1613 °C, 5 % CO₂ tissue culture incubator. Immediately before (T0), 180 min (T180) and 300 min
1614 (T300) after the temperature shift, the medium in the respective well was adjusted to 20 µM
1615 PDS and incubation of cells continued for 9 h to allow for one cycle of infection. Non-infected
1616 cells cultivated in the absence of PDS were examined in parallel. Cells were harvested, fixed,
1617 permeabilised and immunostained with the VP2-specific mAb 8F5, followed by secondary
1618 antibody fluorescently labelled with Alexa Fluor 488 and analysed by flow cytometry. Non-
1619 infected and infected populations are displayed at the left and right, respectively, in the
1620 fluorescence intensity histogram, and the corresponding percentage is provided on top. MFI
1621 is the mean value of fluorescence intensity calculated for each sample.







a**b****c****d****e**

Supplementary Files

This is a list of supplementary files associated with this preprint. Click to download.

- [SupplementaryMaterialFinalNatCommSubmission.docx](#)